



Available online at www.sciencedirect.com

ScienceDirect

Comput. Methods Appl. Mech. Engrg. 413 (2023) 116065

Computer methods in applied mechanics and engineering

www.elsevier.com/locate/cma

Inverse design of magneto-active metasurfaces and robots: Theory, computation, and experimental validation

Chao Wang^a, Zhi Zhao^a, Xiaojia Shelly Zhang^{a,b,c,*}

^a Department of Civil and Environmental Engineering, University of Illinois at Urbana Champaign, 205 North Mathews Ave, Urbana, 61801, IL, USA

^b Department of Mechanical Science and Engineering, University of Illinois at Urbana Champaign, Urbana, 61801, IL, USA ^c National Center for Supercomputing Applications, USA

> Received 16 January 2023; received in revised form 22 March 2023; accepted 12 April 2023 Available online 6 June 2023

Abstract

Magneto-active structures can undergo rapid and reversible deformations under untethered magnetic fields. The capability to design such structures to achieve programmable shape morphing in three dimensions (3D) under magnetic actuation is highly desirable for many applications. In this work, we develop a multi-physics topology optimization framework for the inverse design of magneto-active metasurfaces that can undergo programmable shape morphing in 3D under external magnetic fields. These metasurfaces remain planar in their initial configurations and are deformed into complex 3D target shapes. The proposed framework accounts for large-deformation kinematics and optimizes both the topologies and magnetization distributions of metasurfaces in conjunction with the directions and magnitudes of the external magnetic fields. We demonstrate the framework in the design of kirigami metasurfaces, bio-inspired robots with "swimming", "steering", "walking", and "climbing" motions, and multi-modal magnetic actuators, and the optimized designs show high precision and performance in achieving complex 3D deformations. We also use a hybrid fabrication procedure to manufacture representative designs and conduct experimental tests to validate their programmed 3D deformations, with results showing good agreement with simulation predictions. We envision that the proposed framework could lead to a systematic and versatile approach for the design of magneto-active metasurfaces for robotics applications.

© 2023 Elsevier B.V. All rights reserved.

Keywords: Inverse design; Three-dimensional shape programming; Topology optimization; Magneto-active metasurfaces and robots; Mold casting fabrication; Hard-magnetic soft materials

1. Introduction

Programming two dimensions (2D) structures to achieve complex three dimensions (3D) shape morphing through external stimuli has been a widely studied topic with numerous applications, including soft robotics, foldable structures, and biomedical devices [1]. A range of active materials, such as swellable hydrogels, shape-memory polymers, and liquid crystal elastomers have been explored for the design and fabrication of stimulus-responsive 2D

E-mail address: zhangxs@illinois.edu (X.S. Zhang).

^{*} Corresponding author at: Department of Civil and Environmental Engineering, University of Illinois at Urbana Champaign, 205 North Mathews Ave, Urbana, 61801, IL, USA.

structures for 3D morphing. Among these materials, hard-magnetic soft materials [2,3] composed of soft elastomeric matrices and the embedded hard magnetic particles have received great attention since they can sustain a high remnant magnetization after being magnetically saturated, making them capable of achieving rapid, untethered, and reversible shape transformations under magnetic actuation. Moreover, the direction of the remnant magnetization can be designed over the structure [4], enabling the attainment of various types of shape transformations. The magnetic field stimuli can be applied and controlled remotely, making hard-magnetic soft materials an excellent choice for creating 2D planar structures, such as metasurfaces and robots that can exhibit programmable 3D deformations.

However, the design of programmable planar thin-sheet structures made of hard-magnetic soft materials has largely relied on intuition-based or bio-inspired approaches, which may limit design freedom and the accuracy of achieving complex 3D morphing. Some studies have employed data-driven approaches for inverse design of shape morphing [5] or tunable magneto-mechanical metamaterials [6]. Optimization-based approaches have also been explored for the inverse design of shape-programmable magneto-active soft materials [7,8]. These studies have shown great success in obtaining designs with improved accuracy, and predetermined geometries/topologies are mostly considered. The ability to optimize geometry or topology in the inverse design could potentially enable more complex shape programming tasks by expanding the design space.

Topology optimization [9-11], a powerful approach for designing materials and structures to minimize (or maximize) certain objectives under constraints, has been explored in a wide spectrum of fields, including but not limited to solid mechanics [12-15], fluids [16], and acoustics [17,18]. Some studies have employed the topology optimization approach to design stimuli-responsive structures under multi-physics, such as thermomechanics [19,20], electromechanics [21,22], and magnetics [4,23]. For thermal stimuli, Alacoque et al. [19] established a stress-based multi-material thermomechanical topology optimization framework capable of generating zero or negative thermal expansion microstructures. Xu et al. [20] proposed an efficient dimension reduction level-set topology optimization method for heat conduction problems on manifolds. Ogawa and Yamada [24] introduced an efficient 2D topology optimization framework to design thermal actuators. Athinarayanarao et al. [25] developed a computational inverse design framework based on the evolutionary algorithm to optimize 2D multi-material thermal-active composites that can achieve target shapes. For electrical stimuli, Salas et al. [26] proposed a topology optimization formulation to decide the fiber orientation angles in laminated piezocomposite actuators. The design space and dimensions of the existing studies on the topology optimization of stimuli-responsive materials mostly focus on the linear elasticity regime under 2D. Additionally, few studies conduct experimental validation to verify the computational designs. For magnetic stimuli, which is the focus of this work, few studies utilize topology optimization to inverse design magneto-active materials. For example, Tian et al. [23] introduced a level-set-based topology optimization method to determine the soft matrix distribution of the ferromagnetic soft robots capable of generating out-of-plane deformation under a prescribed magnetic field. The framework is built upon linear elasticity. Zhao et al. [4] proposed a densitybased topology optimization framework aimed at optimizing geometry, magnetization distribution, and the applied magnetic fields simultaneously for magneto-active structures. Their framework accounts for large deformation kinematics but only considers 2D designs with both in-plane deformations and applied magnetic fields. However, a systematic inverse design approach capable of (1) concurrently optimizing topology, magnetization profile, and 3D external magnetic fields over any irregular design domain; (2) achieving complex 3D shape morphing from magneto-active planar structures; and (3) accounting for material nonlinearity and large-deformation kinematics in 3D space has yet to be developed. Furthermore, effective fabrication protocols to realize the topology-optimized designs are underdeveloped and experimental validation of their effectiveness remains unexplored.

This study presents a topology optimization framework for the inverse design of magneto-active metasurfaces, where geometry, remnant magnetization distribution, and applied magnetic fields are simultaneously optimized to achieve programmable 3D complex shape morphing under large deformations. The proposed approach integrates theory, numerical implementation, fabrication, and experimental validation, as shown in Fig. 1. From a theoretical and numerical implementation standpoint, three sets of design variables are introduced to parameterize the entire design, including variations in geometry, remnant magnetization distribution, and applied magnetic fields. A Helmholtz free energy function interpolation is developed to characterize the nonlinear magneto-mechanical responses of a given design using the proposed design variables, based on the validated theory of hard-magnetic soft materials proposed by Zhao et al. [3]. A 3D finite element formulation is employed to solve the resulting nonlinear state equations at each optimization iteration. Along with a consistent sensitivity analysis, the proposed optimization framework can handle a variety of objective functions; in this work, two representative ones are

Theory and Numerical Implementation Optimize for **Inverse Design Metasurfaces Optimized Metasurfaces** out-of-plane deformations Matrix distribution $\overline{\rho}_{e}$ $\bar{\rho}_{e}=1$ (Solid) Design domain Target shape Actuated shape magnetization **Shape Programming Robots Optimized Robots** (Void) Candidate Magnetizations B. Optimized Soft Design domain magnetization matrix Magnetic particles **Magneto-active Actuators Optimized Actuators** Applied magnetic fields $B_{\alpha}^{(l)}$ Actuation mode 1 Actuation mode 2 Actuation mode 1 Actuation mode 2 **Fabrication and Experimental Validation** Hard-magnetic soft material Helmholtz coil

Fig. 1. Illustration of the proposed topology optimization framework for inverse design of magneto-active metasurfaces and robots: theory and numerical implementation; fabrication and experimental validation.

demonstrated: (1) fitting a set of target shapes, and (2) maximizing displacement at multiple locations for improved actuation performance. Through examples of designing shape-morphing metasurfaces, bio-mimic soft robotics, and untethered actuators, the proposed framework is shown to generate magneto-active metasurfaces that achieve programmed 3D deformations with high precision. From a fabrication and experimental validation standpoint, a streamlined procedure for mold casting is introduced to manufacture topology-optimized magneto-active structures with complex geometry and magnetization profiles. Representative optimized designs are successfully fabricated, and experimental tests are conducted on the fabricated designs to validate their performance. The experimentally characterized performance of the optimized designs shows good agreement with computational predictions, with errors no greater than 8% for all tested cases. The experimental footage and simulation results for the deformation of the tested structures are provided in the supplementary video.

The remainder of the paper is organized as follows. Section 2 introduces the nonlinear mechanics model and finite element approximation of hard-magnetic soft materials. Section 3 presents the topology optimization framework for generating magneto-active metasurfaces and robots. Section 4 provides three design examples and experimental validation to demonstrate the effectiveness of the proposed design framework. The concluding remarks are presented in Section 5. Three appendices and one video are provided to supplement the paper. Appendix A presents the

sensitivity analysis of the proposed framework using the adjoint method. Appendix B provides details on the characterization of the elastic behavior of hard-magnetic soft materials. Appendix C presents details on the hybrid fabrication and experimental setup of optimized magneto-active structures. The supplementary video provides the experimental validations for a shape programming robot and a magneto-active actuator.

2. Constitutive model of hard-magnetic soft material and finite element approximation

This section presents the nonlinear mechanics model of hard-magnetic soft materials and discusses its finite element approximation under large deformations. Let us consider a deformable solid occupying a domain Ω in the absence of mechanical body force with the displacement boundary condition $u = \overline{u}$ on Γ_u and traction boundary condition $t = \overline{t}$ on Γ_t , such that $\Gamma_u \cup \Gamma_t = \partial \Omega$ and $\Gamma_u \cap \Gamma_t = \emptyset$. We denote x and X as the position vectors in current and reference configurations, respectively. The deformation of the solid is characterized by a mapping function $x = \chi(X)$. Accordingly, the deformation gradient is defined as $F = \frac{\partial x}{\partial X}$.

The current study employs the nonlinear field theory proposed in [3] to describe the nonlinear mechanics of hard-magnetic soft materials. This model adopts several rational assumptions to simplify the complex magnetomechanical coupling in such materials: (1) The applied magnetic field is assumed to be small (far below the coercive field strength of embedded hard-magnetic particles) with negligible influence on the residual magnetic flux density; (2) The magnetic permeability of the hard-magnetic soft material is assumed to be the same as the vacuum permeability; (3) The applied magnetic flux density is assumed to be a uniform vector. It is also worth mentioning several limitations of this model due to the above-mentioned assumptions. First, the adopted model does not consider the self-interaction among the remnant magnetizations of adjacent members, which can lead to deformations without an external field, especially when designing thin or slender members embedded with opposite magnetization directions. Second, the magnetization in the current configuration is related to the original configuration via the deformation gradient F, which incorporates stretching. However, as demonstrated by Mukherjee et al. [27], the current magnetization is independent of the stretching part of the deformation gradient. In turn, this limitation may lead to unreliable predictions in certain scenarios for large deformations or rotations under large applied magnetic fields [28]. Despite these limitations, we choose to use this model because it significantly reduces the computational cost, making it computationally favorable for iterative topology optimization problems. Our work focuses on a small actuating magnetic field range (< 50 mT) under which the model has been shown to reproduce the corresponding experimental results well [3,27]. Additionally, the experiment is conducted under a nearly uniform actuating magnetic field over the working space through the Helmholtz coil. Under these conditions, the assumptions of the adopted model are rational. However, in cases where the above-mentioned assumptions are violated, more accurate and fully coupled magneto-mechanical models, such as the ones proposed in [27,29,30], should be adopted.

According to Zhao et al. [3], the total Helmholtz free energy of hard-magnetic soft material per unit volume in the reference configuration can be expressed as

$$W(\mathbf{F}, \mathbf{B}_r, \mathbf{B}_a) = W_E(\mathbf{F}) + W_M(\mathbf{F}, \mathbf{B}_r, \mathbf{B}_a), \tag{1}$$

where $W_E(F)$ is the hyperelastic stored-energy function for characterizing the nonlinear elasticity of the solid, B_r is the residual magnetic flux density in the reference configuration, and B_a is the applied magnetic flux density, which is assumed to remain uniform and unchanged during the deformation process. In this work, $W_E(F)$ is taken to be a compressible Lopez-Pamies (LP) model [31] given by

$$W_E(\mathbf{F}) = \sum_{i=1}^n \frac{3^{1-\alpha_i}}{2\alpha_i} \mu_i \left(I_1^{\alpha_i} - 3^{\alpha_i} \right) - \sum_{i=1}^n \mu_i \ln J + \frac{\mu'}{2} (J-1)^2, \tag{2}$$

where $I_1 = \operatorname{tr}(\boldsymbol{C})$ is the first invariant of the right Cauchy–Green deformation tensor $\boldsymbol{C} = \boldsymbol{F}^T \boldsymbol{F}$; J is the determinant of deformation gradient $J = \det \boldsymbol{F}$; α_i (i = 1, 2, ..., n) are real-valued material parameters; μ' and $\mu = \sum_{i=1}^n \mu_i$ are the first and second Lamé constants under the initial state, respectively. In this study, we consider a two-term LP model, i.e., n = 2. The second term of the total Helmholtz free energy, $W_M(\boldsymbol{F}, \boldsymbol{B}_r, \boldsymbol{B}_a)$, represents the magnetic potential energy and is defined as [3]

$$W_M(\mathbf{F}, \mathbf{B}_r, \mathbf{B}_a) = -\frac{1}{\mu_0} (\mathbf{F} \mathbf{B}_r) \cdot \mathbf{B}_a, \tag{3}$$

where $\mu_0 = 1.257 \times 10^{-6}$ H/m is the vacuum (or air) magnetic permeability.

Based on the definition of the total Helmholtz free energy $W(F, B_r, B_a)$, the total first Piola-Kirchoff stress tensor is obtained as

$$\mathbf{P} = \frac{\partial W_E}{\partial \mathbf{F}}(\mathbf{F}) - \frac{1}{\mu_0} \mathbf{B}_a \otimes \mathbf{B}_r,\tag{4}$$

where \otimes denotes the tensor product, and we have

$$\frac{\partial W_E}{\partial \mathbf{F}}(\mathbf{F}) = \sum_{i=1}^n \frac{3^{1-\alpha_i}}{\mu_i} I_1^{(\alpha_i - 1)} \mathbf{F} - \sum_{i=1}^n \mu_i \mathbf{F}^{-T} + \frac{\mu'}{J} (J - 1) \mathbf{F}^{-T},$$
 (5)

for the compressible LP model.

We adopt the standard displacement-based finite element method [32] to numerically solve the magnetomechanical boundary value problem. The domain of interest is discretized by a 3D finite element mesh consisting of first-order continuum finite elements (e.g., eight-node hexahedral finite element). Adopting a total Lagrangian formulation, the total potential energy associated with the discretized system is given by

$$\Pi(\boldsymbol{u}) = \sum_{e} \int_{\Omega_{e}} W(\boldsymbol{F}(\boldsymbol{u}_{e}), \boldsymbol{B}_{r}, \boldsymbol{B}_{a}) d\boldsymbol{X} - \boldsymbol{F}_{\text{ext}} \cdot \boldsymbol{u},$$
(6)

where Ω_e denotes a generic finite element e, u_e is the displacement field of element e interpolated from Lagrangian shape functions, u is the global displacement vector, and \mathbf{F}_{ext} is the external force vector obtained from discretizing the traction on the boundary. Minimizing the total potential energy $\Pi(u)$ with respect to the global displacement vector u gives the discretized stationary condition

$$\mathbf{R}(u) = \frac{\partial \Pi}{\partial u}(u) = \mathbf{F}_{\text{int}}(u) - \mathbf{F}_{\text{ext}} = \mathbf{0},\tag{7}$$

which governs the equilibrium of the discretized system. We refer to $\mathbf{R}(u)$ and \mathbf{F}_{int} as the global residual vector and global internal force vectors, respectively. In this work, the nonlinear Eq. (7) is solved using the Newton-Raphson method [32] with the inexact line search method [33,34]. This nonlinear solver makes use of consistently linearized tangent stiffness matrices, for which we apply the "fsparse" routine [35,36] to enhance the computational efficiency of sparse matrix assembly.

3. Topology optimization framework for magneto-active metasurface design

In this section, we introduce the topology optimization framework for inversely designing magnetoactive metasurfaces and robots to achieve complex deformations and motions in the 3D space. The design framework builds upon the 2D optimization framework proposed by Zhao et al. [4]. Since this work aims to achieve complex 3D deformation and actuation mechanisms with hard-magnetic soft material metasurfaces and robots, we highlight several key techniques developed to achieve this goal. First, we introduce a design parameterization scheme that can represent the design spaces of 3D topology, in-plane magnetization distribution, and varying applied magnetic fields in 3D. In addition, a 3D finite element model is developed to solve the nonlinear state problem arising from material nonlinearity and large deformation. Second, we introduce a projection-based approach to ensure planar metasurface designs and enforce uniform density and magnetization along the out-of-plane direction, which is an important manufacturing consideration for realizing those designs. Third, we extend our computational framework to handle unstructured meshes and irregular design domains in 3D, enhancing the versatility and applicability of the method. Last but not least, we develop a tailored fabrication approach and conduct experimental validation of the optimized magneto-active structures. Comparisons between the numerical and experimental results validate the effectiveness and accuracy of our proposed design methodology. Overall, these technical advancements facilitate the realization of our proposed design methodology and demonstrate the potential of our magneto-active designs for various applications. In the following, we first explain how to parameterize magneto-active metasurface designs using design variables and then present the general optimization formulation.

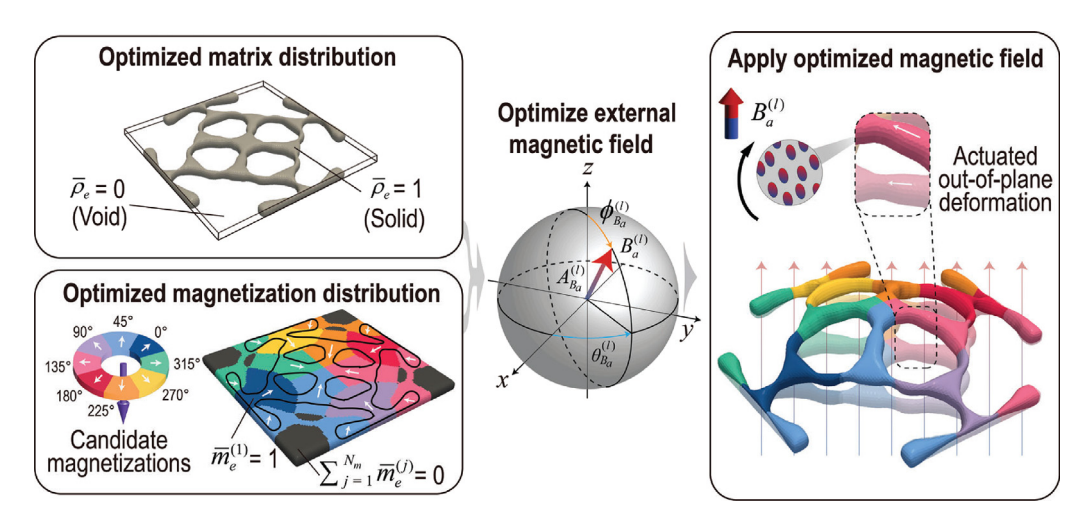


Fig. 2. Illustration of the parameterization scheme.

3.1. Design parameterization of magneto-active metasurfaces

Our framework utilizes three sets of physical variables to enable the simultaneous optimization of geometry, remnant magnetization, and external magnetic fields. Considering a magneto-active design as schematically illustrated in Fig. 2, we use the physical density variables, denoted by $\overline{\rho}$, to parameterize its material distribution (i.e., geometry), and employ the magnetization indicator variables, denoted by vectors \overline{m}_i , $i=1,\ldots,N_m$, to parameterize its underlying distribution of magnetization (such that the magnetization at each location is determined from N_m candidate orientations). In addition, we also introduce vectors $B_a^{(\ell)}$, to represent the external magnetic field necessary to achieve the ℓ th target spatial deformation. Combined, the physical density variables $\overline{\rho}$ and magnetization indicator variables \overline{m}_i determine what the magneto-active design will look like. The spatial vectors $B_a^{(\ell)}$, on the other hand, inform how we shall control the external magnetic fields to ensure that the target deformations will be actuated. We highlight that parameterizing geometry, remnant magnetization distribution, and external magnetic fields separately allow us to flexibly consider only a subset of the design space within the proposed framework without any modification. For example, if one wants to fix the geometry of the design and only optimize the magnetization profile and external fields, one can achieve that by simply treating the density variables $\overline{\rho}$ as non-designable fields and optimizing the remaining variables.

How each set of physical variables is mapped and constructed from their respective design variables is described in detail below. In the discussions, we assume that the design domain is already discretized by a finite element mesh Ω_h composed of N_e elements.

Parameterization of material distribution. The physical density vector $\overline{\rho}$ is used to represent the material distribution (i.e., geometry) of the design. Its eth component $\overline{\rho}_e \in [0,1]$ is used to indicate the material distribution of element e with $\overline{\rho}_e = 1$ and $\overline{\rho}_e = 0$ indicating solid and void, respectively. The physical density vector $\overline{\rho}$ is obtained from the density design variable vector ρ via a procedure combining Heaviside projection and filtering. To promote black-and-white designs, the physical density $\overline{\rho}_e$ is defined as the projection of an intermediate variable $\widetilde{\rho}_e$ via a smoothed Heaviside function [37] as

$$\overline{\rho}_e = \frac{\tanh(\frac{\beta_\rho}{2}) + \tanh(\beta_\rho(\widetilde{\rho}_e - \frac{1}{2}))}{\tanh(\frac{\beta_\rho}{2}) + \tanh(\beta_\rho(1 - \frac{1}{2}))},\tag{8}$$

where β_{ρ} is the discreteness parameter ($\beta_{\rho} = 1, 2, 4, ..., 64$ doubled every 40 optimization iterations). To avoid checkerboard instability and impose minimum length scale, the intermediate variable $\widetilde{\rho}_{e}$ is subsequently obtained from the density design variables ρ_{i} via a filtering [38] procedure

$$\widetilde{\rho}_e = \frac{\sum_{i \in \mathscr{I}_e(R_\rho)} w_i v_i \rho_i}{\sum_{i \in \mathscr{I}_e(R_\rho)} w_i v_i},\tag{9}$$

where $\mathscr{I}_e(R_\rho)$ is the set of indices of elements whose centroids fall within the filter radius of R_ρ from the centroid of the eth element (denoted as X_e), namely $\mathscr{I}_e(R_\rho) = \{i : \|X_i - X_e\| \le R_\rho\}$, v_i is the volume of the ith element, and w_i is the weighting factor calculated by $w_i = 1 - (\|X_i - X_e\| / R_\rho)$. Composing relations (8) with (9) gives the mapping from ρ to $\overline{\rho}$.

Parameterization of non-uniform magnetization distribution. In our parameterization, we first predefine a set of candidate magnetic flux density vectors $\{B_r^{(1)}, \ldots, B_r^{(N_m)}\}$. For the metasurface designs featured in this work, we define these candidate remnant magnetic flux density vectors as eight in-plane directions that are 45° apart from one another, with the same magnitude. The final magnetization vectors at each element will be selected by the optimization formulation from these candidate magnetic flux density vectors to minimize/maximize the objective function, which essentially forms a multi-component or multi-material parameterization problem [39–43]. To achieve this, we introduce a set of magnetization indicator variable vectors \overline{m}_i , $i = 1, \ldots, N_m$ and represent the actual residual magnetic flux density $B_{r,e}$ associated with element e as

$$\boldsymbol{B}_{r,e} = \sum_{i=1}^{N_m} \left(\overline{m}_e^{(j)} \right)^{p_m} \boldsymbol{B}_r^{(j)}, \tag{10}$$

where $\overline{m}_e^{(j)}$ is the *e*th component of vector \overline{m}_j and p_m is a penalization parameter. From the above definition, it can be seen that $\overline{m}_e^{(i=j)} = 1$ and $\overline{m}_e^{(i\neq j)} = 0$ indicate the *j*th candidate magnetic flux density $\boldsymbol{B}_r^{(j)}$ is selected for element *e*. Because the magnetization indicator variables can continuously vary from 0 to 1, choosing $p_m > 1$ penalizes intermediate values of those indicator variables to make them unfavorable for optimization.

To ensure Eq. (10) have physical meaning, we require $\overline{m}_e^{(j)} \ge 0$, $\forall j$ and $\sum_{j=1}^{N_m} \overline{m}_e^{(j)} \le 1$ (we note that allowing the summation to be smaller than 1 makes it possible that element e is non-magnetized). To satisfy both conditions, we define $\overline{m}_e^{(j)}$, $j=1,\ldots,N_m$ as projections from a set of magnetization design variables $\xi_e^{(j)} \in [0,1]$, $j=1,\ldots,N_m$ and adopt the Hypercube-to-Simplex Projection (HSP) scheme [39,40] to realize this mapping. Using the HSP scheme, the magnetization indicator variable $\overline{m}_e^{(j)}$ in element e is expressed as

$$\overline{m}_e^{(j)} = \sum_{i=1}^{2^{N_m}} s_i^{(j)} \left((-1)^{\left(N_m + \sum_{j=1}^{N_m} c_i^{(j)}\right)} \prod_{k=1}^{N_m} \left(\overline{\xi}_e^{(k)} + c_i^{(k)} - 1 \right) \right), \tag{11}$$

where $c_i^{(j)} \in \{0, 1\}$ is the *j*th component of the *i*th vertex of an N_m -dimensional unit hypercube; and $s_i^{(j)}$ is the projected vertex of $c_i^{(j)}$ to an N_m -dimensional standard simplex domain:

$$s_i^{(j)} = \begin{cases} \frac{c_i^{(j)}}{\sum_{j=1}^{N_m} c_i^{(j)}} & \text{if } \sum_{j=1}^{N_m} c_i^{(j)} \ge 1, \\ 0 & \text{otherwise.} \end{cases}$$
 (12)

The variables $\overline{\xi}_e^{(j)}$, $j=1,\ldots,N_m$ used in Eq. (11) are obtained by applying the Heaviside projection and filtering operations (as given by Eqs. (8) and (9), respectively) on the magnetization design variables $\xi_e^{(j)}$, $j=1,\ldots,N_m$ [4]. The associated filter radius and discreteness parameters are denoted as R_m and β_m , respectively.

Parameterization of external magnetic fields. Being able to actuate 3D deformations requires parameterization of applied external magnetic flux density B_a in the 3D space. Assuming the design is operated under a total of N_{ℓ} magnetic fields with various magnitudes and orientations, we parameterize them as

$$\boldsymbol{B}_{a}^{(\ell)} = \begin{bmatrix} A_{B_{a}}^{(\ell)} \sin\left(\phi_{B_{a}}^{(\ell)}\right) \cos\left(\theta_{B_{a}}^{(\ell)}\right) \\ A_{B_{a}}^{(\ell)} \sin\left(\phi_{B_{a}}^{(\ell)}\right) \sin\left(\theta_{B_{a}}^{(\ell)}\right) \\ A_{B_{a}}^{(\ell)} \cos\left(\phi_{B_{a}}^{(\ell)}\right) \end{bmatrix}, \tag{13}$$

where the index ℓ represents the ℓ th applied magnetic field. The design variables associated with such a parameterization are $A_{B_a}^{(\ell)} \in [0, A_{B_a, \max}^{(\ell)}], \phi_{B_a}^{(\ell)} \in [0, \pi]$, and $\theta_{B_a}^{(\ell)} \in [0, 2\pi]$ representing the magnitude, the elevation angle, and the polar angle of those applied magnetic fields.

Magneto-mechanical behavior of parameterized designs. For any parameterized design, it is necessary to simulate its magneto-mechanical behavior in order to obtain design sensitivities. Such simulations require the interpolation of Helmholtz free energy function from the physical variables described above. Let us consider a generic finite element e whose physical density and residual magnetic flux density are $\overline{\rho}_e$ and $\boldsymbol{B}_{r,e}$, respectively, the latter of which are interpolated from the magnetization indicator variables $\overline{m}_e^{(j)}$, $j=1,\ldots,N_m$ (see Eq. (10)). The interpolated Helmholtz free energy function associated with that element under the ℓ th parameterized applied magnetic flux density $\boldsymbol{B}_e^{(\ell)}$ is given by [4]

$$W_{e}\left(\overline{\rho}_{e}, \overline{m}_{e}^{(1)}, ..., \overline{m}_{e}^{(N_{m})}, \boldsymbol{B}_{a}^{(\ell)}, \boldsymbol{u}_{e}^{(\ell)}\right) = \left[\epsilon + (1 - \epsilon)\left(\overline{\rho}_{e}\right)^{p_{\rho}}\right] W_{E}\left(\boldsymbol{F}(\boldsymbol{u}_{e}^{(\ell)})\right) - \frac{(\overline{\rho}_{e})^{p_{\rho}}}{\mu_{O}} \left[\boldsymbol{F}(\boldsymbol{u}_{e}^{(\ell)})\boldsymbol{B}_{r,e}(\overline{m}_{e}^{(1)}, ..., \overline{m}_{e}^{(N_{m})})\right] \cdot \boldsymbol{B}_{a}^{(\ell)},$$

$$(14)$$

where $u_e^{(\ell)}$ is the displacement vector of element e induced by the applied magnetic flux density $B_a^{(\ell)}$, and ϵ is a small value assigned to the void regions to prevent the singularity of the stiffness matrix. The Solid Isotropic Material with Penalization (SIMP) approach [9,44] is applied to both the mechanical hyperelastic energy and magnetic potential energy with the same penalization parameter p_ρ to promote black-and-white designs. In addition, the low-density regions under large deformation can cause severe numerical instability that needs to be tackled [45] or circumvented [46,47]. In this study, we employ the energy interpolation scheme proposed by Wang et al. [45] for the mechanical hyperelastic energy to tackle the numerical instability problem.

Having defined the interpolated Helmholtz free energy for a generic element, the total potential energy of a parameterized design under external magnetic field $\mathbf{B}_a^{(\ell)}$ becomes

$$\Pi(\overline{\boldsymbol{\rho}}, \overline{\boldsymbol{m}}^{(1)}, \dots, \overline{\boldsymbol{m}}^{(N_m)}, \boldsymbol{B}_a^{(\ell)}, \boldsymbol{u}^{(\ell)}) = \sum_{e} \int_{\Omega_e} W_e\left(\overline{\rho}_e, \overline{m}_e^{(1)}, \dots, \overline{m}_e^{(N_m)}, \boldsymbol{B}_a^{(\ell)}, \boldsymbol{u}_e^{(\ell)}\right) d\boldsymbol{X} - \mathbf{F}_{\text{ext}} \cdot \boldsymbol{u}. \tag{15}$$

Following the same procedure of minimizing this total potential energy with respect to u, we obtain the discretized stationary condition for the parameterized design under the applied magnetic field $B_a^{(\ell)}$ as

$$\frac{\partial \Pi}{\partial \boldsymbol{u}}(\overline{\boldsymbol{\rho}}, \overline{\boldsymbol{m}}^{(1)}, \dots, \overline{\boldsymbol{m}}^{(N_m)}, \boldsymbol{B}_a^{(\ell)}, \boldsymbol{u}^{(\ell)}) = \mathbf{R}(\overline{\boldsymbol{\rho}}, \overline{\boldsymbol{m}}^{(1)}, \dots, \overline{\boldsymbol{m}}^{(N_m)}, \boldsymbol{B}_a^{(\ell)}, \boldsymbol{u}^{(\ell)}) = \mathbf{0}, \tag{16}$$

which is adopted by the proposed framework to solve the magneto-mechanical behavior at each topology optimization iteration.

3.2. Topology optimization formulation

This subsection introduces a general topology optimization formulation for magneto-active metasurface designs. Consider a finite element Ω_h mesh and assume there are N_m candidate magnetizations and N_ℓ operating applied magnetic fields. The topology optimization formulation is given by

$$\min_{\boldsymbol{\rho},\boldsymbol{\xi}^{(1)},\dots,\boldsymbol{\xi}^{(N_m)},\\ \boldsymbol{B}_a^{(1)},\dots,\boldsymbol{B}_a^{(N_\ell)}} f\left(\boldsymbol{u}^{(1)},\dots,\boldsymbol{u}^{(N_\ell)}\right),$$
s.t.:
$$\frac{\boldsymbol{v}^T \overline{\boldsymbol{\rho}}}{|\Omega_h|} \leq v_{\text{max}},$$

$$\left\{ \sum_{e=1}^{N_e} \left[\frac{w_{\sigma}(\overline{\rho}_e)}{v_e} \int_{\Omega_{h,e}} \sigma_{\text{VM}} \left(\boldsymbol{\sigma}_E \left(\boldsymbol{u}^{(\ell)} \right) \right) d\boldsymbol{X} \right]^{p_n} \right\}^{1/p_n} \leq \sigma_{\text{max}}^{(\ell)}, \quad \ell = 1,\dots, N_\ell,$$

$$\mathbf{R}(\overline{\boldsymbol{\rho}}, \overline{\boldsymbol{m}}^{(1)}, \dots, \overline{\boldsymbol{m}}^{(N_m)}, \boldsymbol{B}_a^{(\ell)}, \boldsymbol{u}^{(\ell)}) = \boldsymbol{0}, \quad \ell = 1,\dots, N_\ell,$$

$$\boldsymbol{0} \leq \boldsymbol{\rho} \leq \boldsymbol{1},$$

$$\boldsymbol{0} \leq \boldsymbol{\xi}^{(j)} \leq \boldsymbol{1}, \quad j = 1,\dots, N_m,$$

$$0 \leq A_{B_a}^{(\ell)} \leq A_{B_a, \text{max}}^{(\ell)}, \quad \ell = 1,\dots, N_\ell,$$

$$0 \leq \theta_{B_a}^{(\ell)} \leq 2\pi, \quad \ell = 1,\dots, N_\ell,$$

$$0 \leq \phi_{B_a}^{(\ell)} \leq \pi, \quad \ell = 1,\dots, N_\ell,$$

where \mathbf{v} is a vector collecting element volumes with its eth component v_e being the volume of element e, and v_{max} is the prescribed maximum volume fraction. The general setting of the formulation allows the three sets of design variables ρ , $\boldsymbol{\xi}^{(j)}$, and $\boldsymbol{B}_a^{(\ell)}$ to be optimized either simultaneously or partially (with those non-designable portions prescribed as constant during optimization). To eliminate thin members and limit excessive local deformations in optimized designs, we introduce an aggregated von Mises stress constraint [4,48–51] (using the p-norm approximation with the factor p_n) for each applied magnetic field. The element-level von Mises stress σ_{VM} is computed from the mechanical part of the Cauchy stress σ_E . The stress relaxation approach [50] is adopted giving $w_{\sigma}(\overline{\rho}_e) \doteq \epsilon + (1 - \epsilon)\overline{\rho}_e^q$ with q being 1/2.

The proposed formulation (17) can take any form of objective functions. This work considers two representative ones, as described below. The first objective function aims to generate metasurface designs to realize a set of target deformed shapes:

$$f_1\left(\boldsymbol{u}^{(1)}, \dots, \boldsymbol{u}^{(N_\ell)}\right) = \max_{\ell \in \{1, \dots, N_\ell\}} \left(\frac{1}{N_\alpha^{(\ell)}} \sum_{\alpha=1}^{N_\alpha^{(\ell)}} \left(\frac{u_\alpha^{(\ell)} - u_\alpha^{*(\ell)}}{u_\alpha^{*(\ell)}} \right)^2 \right). \tag{18}$$

The second objective function, which aims to maximize the actuated displacement of certain regions of the design, is expressed as

$$f_2(\boldsymbol{u}^{(1)}, \dots, \boldsymbol{u}^{(N_{\ell})}) = \max_{\substack{\ell \in \{1, \dots, N_{\ell}\}\\ \alpha \in \{1, \dots, N_{\alpha}^{(\ell)}\}}} u_{\alpha}^{(\ell)}.$$
(19)

For both objective functions, $u_{\alpha}^{(\ell)}$ is the actual displacement at the α th control degree of freedom (DOF) of the metasurface under applied magnetic field $\boldsymbol{B}_{a}^{(\ell)}$; $u_{\alpha}^{*(\ell)}$ denotes the associated target displacement at this control DOF; and $N_{\alpha}^{(\ell)}$ stands for the total number of the control DOFs.

The optimization problem is solved by the method of moving asymptotes (MMA) [52]. The maximum operators in those objective functions are handled by the bound formulation [53]. The sensitivity information of the objective and constraint functions with respect to the design variables are derived by the adjoint method [9] and chain rule. Readers are referred to Appendix A for the details of the sensitivity analysis.

3.3. Framework summary

We present the algorithm to show the computational procedures of the proposed multiphysics topology optimization framework. In Algorithm 1, i refers to the ith optimization iteration, i_{max} is the number of optimization iterations, Δ_0 is the convergence toleration, and Δ is the maximum absolute change of design variables.

Algorithm 1 Topology optimization framework for magneto-active metasurface design

```
Set up design and optimization parameters Initialize: \rho, \xi, B_a, i=0 while i \leq i_{\max} and \Delta > \Delta_0 do i=i+1 \widetilde{\rho} \leftarrow \rho and \widetilde{\xi} \leftarrow \xi via Eq. (9) \overline{\rho} \leftarrow \widetilde{\rho} and \xi \leftarrow \xi via Eq. (8) \overline{m} \leftarrow \widetilde{\xi} via Eq. (11) obtain u by minimizing \Pi(\overline{\rho}, \overline{m}, B_a, u) (Eq. (15)) via nonlinear finite element analysis under large deformations f_1 or f_2 \leftarrow u via Eq. (18) or Eq. (19), respectively evaluate volume and stress constraints in Formulation (17) sensitivity analysis (see Appendix A) update design variables \rho, \xi, and B_a via MMA [52] change p_\rho, p_m, \beta_\rho, and \beta_m at prescribed steps \Delta = \max(|(\rho^i, \xi^i) - (\rho^{i-1}, \xi^{i-1})|) end while
```

4. Exemplar designs of magneto-active metasurfaces and robots

This section presents three design examples of magneto-active metasurfaces and robots to demonstrate the effectiveness of the topology optimization framework. In Example 1, we aim to program various target out-of-plane shapes into Kirigami metasurfaces by optimizing magnetization distributions under prescribed applied magnetic fields. In Example 2, spider-inspired robots are designed by simultaneously optimizing the magnetization distribution and the applied magnetic fields to achieve quasi-static motions by varying the applied magnetic fields. In Example 3, we optimize the matrix and magnetization distributions to generate multi-functional actuators that can achieve programmable 3D (both in-plane and out-of-plane) multi-modal deformation.

We use objective function $f_1(\cdot)$ (Eq. (18)) for Examples 1 and 2 and objective function $f_2(\cdot)$ (Eq. (19)) for Example 3. The parameters of hard-magnetic soft materials in all the examples are selected within a reasonable range based on the experimentally measured data and from the literature [3,54].

To physically validate the proposed framework, we realize optimized designs obtained from Examples 2 and 3 via a mold casting approach and conduct experimental tests of manufactured designs to confront our numerical results. Details on the fabrication procedure and experimental setup are provided in Appendix C.

4.1. Kirigami metasurfaces

We design three magneto-active kirigami metasurfaces to achieve various target out-of-plane deformations by optimizing the magnetization distribution under prescribed magnetic fields. The design domain is taken to be a circular sheet with a pair of spiral cuts as shown in Fig. 3(a). The thickness of the metasurfaces is 2 mm. The paths of the two spiral cuts are defined by the functions $r = \pm \theta^2$ ($\theta \in [1.5\pi, 6\pi]$) under the polar coordinate system with r and θ being radius and angle, respectively. The width of the cuts is 2 mm. The design domain is supported at its outer boundary and discretized using 4,448 8-node hexahedral finite elements.

The elastic behavior of the material is characterized by the compressible LP hyperelastic model (Eq. (2)) with the parameters $\alpha_1 = 2.9798$, $\alpha_2 = -0.0783$, $\mu_1 = 0.0276$ MPa, and $\mu_2 = 0.1478$ MPa (the corresponding initial shear modulus is $\mu = 0.1754$ MPa). To alleviate the volumetric locking issue in the finite element analysis, the Poisson's ratio is set as $\nu = 0.49$. In this example, the physical density variables ρ remain to be solid (i.e., $\rho = 1$) throughout the design domains. We set $N_m = 8$ candidate magnetization vectors distributed in the x-y plane, which are apart from each other with 45° as shown in Fig. 3(a). The initial guess of the remnant magnetization is set to be evenly distributed along the candidate magnetization vectors, that is, $\xi_e^{(j)} = 1/N_m$, $j = 1, \ldots, N_m$. The magnitudes of those candidate magnetization vectors are set to be 100 mT. We note that non-magnetized regions are also allowed to appear in the design.

To ensure the manufacturability of optimized metasurfaces, the distributions of magnetization are taken to be the same along the thickness direction (the z-direction) [55]. In addition, we divide the in-plane design domain into several subdomains, as shown in Fig. 3(a), and enforce the magnetization direction to be uniform within each subdomain [4].

As depicted in Fig. 3(b), we generate three magneto-active kirigami metasurfaces to realize three different target shapes under the prescribed external magnetic fields pointing in the positive z-direction with different magnitudes. To evaluate the fitting accuracy of those optimized designs, we define a normalized relative error as:

Fitting error =
$$\max_{\ell \in \{1, ..., N_{\ell}\}} \left(\frac{1}{N_{\alpha}^{(\ell)}} \sum_{\alpha=1}^{N_{\alpha}^{(\ell)}} \left| \frac{u_{\alpha}^{(\ell)} - u_{\alpha}^{*(\ell)}}{u_{\alpha}^{*(\ell)}} \right| \right),$$
 (20)

where $N_{\ell} = 1$ in this example.

In Case 1, the center of the metasurface is controlled to achieve a target displacement of 18 mm in the positive z-direction. We can observe a spring-like deformation forming under the magnetic actuation. The fitting error is evaluated as 5.60%, indicating the high accuracy of this design. Interestingly, the magnetization direction is observed to follow a clockwise pattern along the spiral path. This clockwise pattern, coupled with the tendency of magnetized members to be aligned with the direction of the applied magnetic field due to magnetic torque and bending, enables the metasurface to be pulled up like a spring. In Case 2, three DOFs are controlled to achieve a target shape with directionally alternating displacements, as shown in Fig. 3(b). We can observe the optimized magnetization directions are distributed in a counterclockwise direction along the two spiral paths. Under the applied magnetic

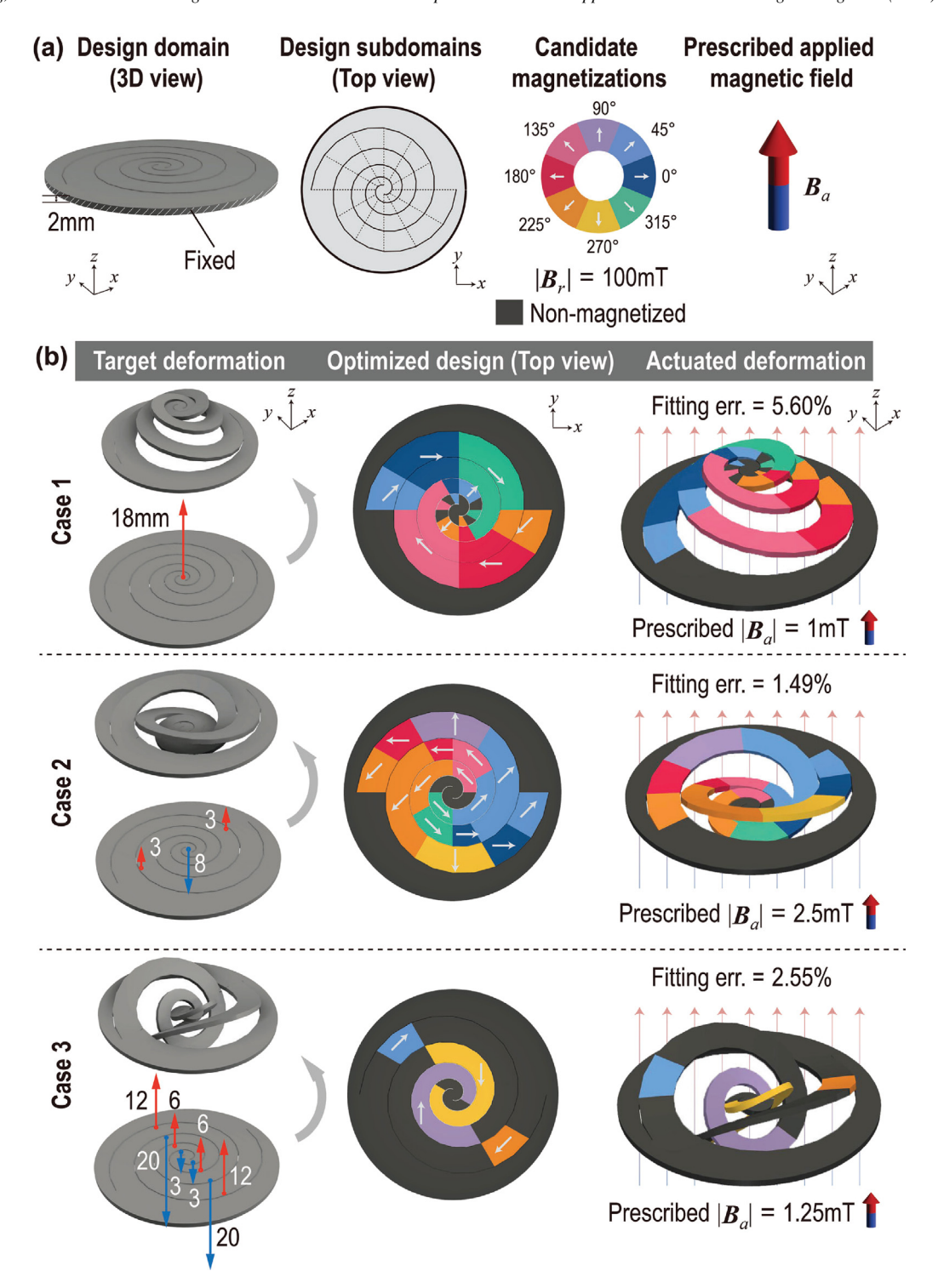


Fig. 3. Shape programming metasurfaces: (a) Design domain (subdomains), candidate magnetization vectors, and prescribed applied magnetic field; (b) Target deformation, optimized design, and actuated deformation.

field, the generated magnetic torque bends the outer two control DOFs upward while pushing the central control DOF downward simultaneously. The target shape can be successfully achieved with an error of 1.49%. Based on the

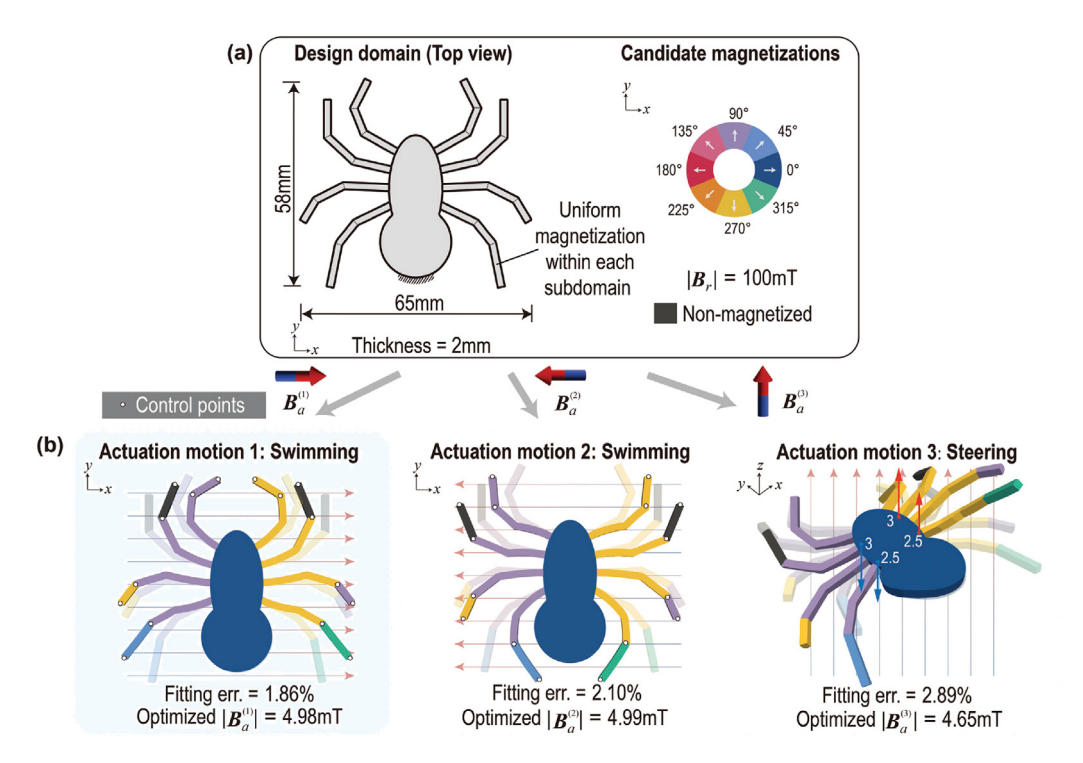


Fig. 4. Spider-inspired shape programming robot with "swimming" and "steering" modes: (a) Design domain and candidate magnetization vectors; (b) Target and actual motions under the optimized magnetic actuations.

setup and design in Case 2, we assign more control DOFs to generate a more complex target shape with alternating deformation directions. The design result shows that such a complex target shape can be accurately achieved (with a fitting error of 2.55%) even with relatively fewer magnetization directions existing in the design.

We remark that all three cases of this example showcase symmetric patterns of the magnetization distribution with respect to the center. This design principle is used in the existing intuition-based designs (e.g., [56]). Notably, our topology optimization framework can bring in further improvements, such as higher preciseness and more flexibility to achieve complex deformation shapes for this type of metasurface designs. We also note that large out-of-plane deformations can be actuated by relatively smaller external magnetic fields compared to the in-plane ones, the latter of which sometimes require 50 mT or larger magnetic fields [4]. This can be explained by metasurfaces typically having smaller out-of-plane stiffnesses than in-plane ones.

4.2. Spider-inspired shape programming robots

In this example, we consider the inverse design of two spider-inspired robots that are optimized to accurately achieve quasi-static motions under changing magnetic fields. The robots are designed by optimizing both their magnetization distributions and the external magnetic fields simultaneously. The design domain of the robots is a spider-like geometry with four pairs of legs and a main body, as shown in Fig. 4(a). The design domain is discretized using 5,448 8-node hexahedral finite elements.

The elastic behavior of magneto-active material is modeled by a compressible LP hyperelastic model with the parameters $\alpha_1 = 2.9798$, $\alpha_2 = -0.0783$, $\mu_1 = 0.0276$ MPa, and $\mu_2 = 0.1478$ MPa, which lead to the shear modulus $\mu = 0.1754$ MPa. The Poisson's ratio is set as $\nu = 0.49$. The objective function $f_1(\cdot)$ (i.e., Eq. (18)) is adopted. The physical density variables ρ remain to be solid (i.e., $\rho = 1$) throughout the optimization.

We aim to realize two application scenarios, each of which involves two types of motions: (1) swimming and steering; (2) walking and climbing. For each scenario, we apply the proposed framework to design a magneto-active robot that realizes the corresponding motions under various external magnetic fields. To ensure manufacturability, we divide the design domain into subdomains as shown in Fig. 4(a), and the magnetization within each subdomain

is set to be uniform. For both design scenarios, the magnitudes of the candidate magnetization vectors are all set to be 100 mT, and non-magnetized regions are allowed to appear in the design. The initial magnetization design variables are set to be uniformly distributed among the 8 candidate vectors within each finite element, i.e., $\xi_e^{(j)} = 1/8$, j = 1, ..., 8. We evaluate the accuracy of the inverse design according to Eq. (20) with $N_{\ell} = 3$.

4.2.1. A robot realizing swimming and steering motions

In the first scenario, we plan to optimize the magnetization distribution of a robot to enable it to perform three quasi-static motions under three applied magnetic fields, which are concurrently optimized as well. The first two motions, associated with applied fields $B_a^{(1)}$ and $B_a^{(2)}$, work together to achieve the swimming locomotion mode, while the third motion, associated with the applied field $B_a^{(3)}$, corresponds to the steering mode. The swimming mode is realized by the deformation of the legs, while the steering mode is driven by the deformation of the body. The control points and the target shapes are shown in Fig. 4(b). To ensure symmetric deformations with respect to the y-axis for the swimming mode, we apply a pair of opposite magnetic fields for the first two quasi-static motions that work collaboratively to achieve the swimming mode. These fields are pointing right ($\theta_{B_a}^{(1)} = 0$ and $\phi_{B_a}^{(1)} = \pi/2$) and left ($\theta_{B_a}^{(1)} = \pi$ and $\phi_{B_a}^{(1)} = \pi/2$), respectively, and the remnant magnetization direction of the body part is fixed towards the left. We define 8 in-plane candidate magnetization vectors that are 45° apart from each other, as shown in Fig. 4(a). The maximum magnitudes of the applied magnetic fields $A_{B_a, \max}^{(\ell)}$, $\ell = 1, \ldots, 3$ are set as 5 mT. The initial magnitudes of the applied magnetic fields are set as $A_{B_a, \max}^{(\ell)}$, $\ell = 1, \ldots, 3$.

The optimized magnetization distribution, the optimized magnitudes of the applied magnetic fields, and the actual deformations under $\mathbf{B}_a^{(\ell)}$, $\ell=1,2,3$ are shown in Fig. 4(b). The fitting error is quantified as 2.89% according to Eq. (20). These results suggest that the optimized magnetization distribution can achieve complex deformation modes with high precision. The legs are actuated to move forward and backward under the first two opposite applied magnetic fields, storing and releasing energy to drive the spider robot to swim. The out-of-plane applied magnetic field $\mathbf{B}_a^{(3)}$ leads the body to deform out-of-plane, allowing the spider robot to change its moving direction.

4.2.2. A robot realizing walking and climbing modes

To further demonstrate the capability of programming 3D out-of-plane shapes, we investigate a second scenario, where we program three quasi-static motions to achieve "walking" and "climbing" modes. We not only optimize the magnetization distribution and magnitude of the three external magnetic fields but also the direction of the applied magnetic field for the third shape. The "walking" locomotion is realized by programming the deformation of the legs. The control points and the target movements are shown in Fig. 5(b). To mimic the coordinated walking mechanism of a spider, we divide the legs into two groups. Under the actuation of the first magnetic field $B_a^{(1)}$, the first group of legs is lifted, while the other group moves downward. Under the actuation of the second magnetic field $B_a^{(2)}$, the movement of the two groups of legs is reversed. The "walking" motion of the robot can be realized by applying the first and second magnetic fields alternatively. The "climbing" of the robot is realized by controlling the deformation of the body. As in the first design scenario, we fix the directions of the associated applied magnetic fields to be upward (i.e., $\phi_{B_a}^{(1)} = 0$ and $\theta_{B_a}^{(1)} = 0$) and downward (i.e., $\phi_{B_a}^{(2)} = \pi$ and $\theta_{B_a}^{(2)} = 0$) to enable symmetric deformations with respect to the y-direction for target shapes 1 and 2. We set the residual magnetization of the central body to be a constant vector with a magnitude of 100 mT and pointing downward. The candidate magnetization directions for the legs are defined in the same way as in the first scenario. The maximum magnitudes of the applied magnetic fields $A_{B_a, \max}^{(\ell)}$, $\ell = 1, \ldots, 3$ are set to 5 mT, and the initial magnitudes are set to half of the maximum. The initial direction of the third magnetic field is prescribed as $\phi_{B_a}^{(3)} = \pi/2$.

The optimized results, including the remnant magnetization and the three applied magnetic fields, are shown in Fig. 5(b). The maximum fitting error is quantified as 10.72%. By alternatively switching between the magnetic fields $B_a^{(1)}$ and $B_a^{(2)}$, the optimized robot can be actuated from a planar configuration to achieve the "walking" motion. The "climbing" motion is realized by the out-of-plane bending of the main body under the applied magnetic field $B_a^{(3)}$, as shown in Fig. 5(b). To validate these numerical results, we manufacture the optimized robot using a mold casting approach [57] (see the detailed description of this approach in Appendix C). The applied magnetic fields are generated by a pair of Helmholtz coils. As shown in Fig. 5(c), under the actuation of the three optimized magnetic fields, the fabricated robot deforms in a consistent way with the numerical results. By alternating the direction of the magnetic fields from $B_a^{(1)}$ to $B_a^{(2)}$, the four pairs of "legs" are lifted in the air or struck down to the ground alternatively to mimic the "walking" motion. By changing the applied magnetic field to $B_a^{(3)}$, the motion switches to the "climbing" mode.

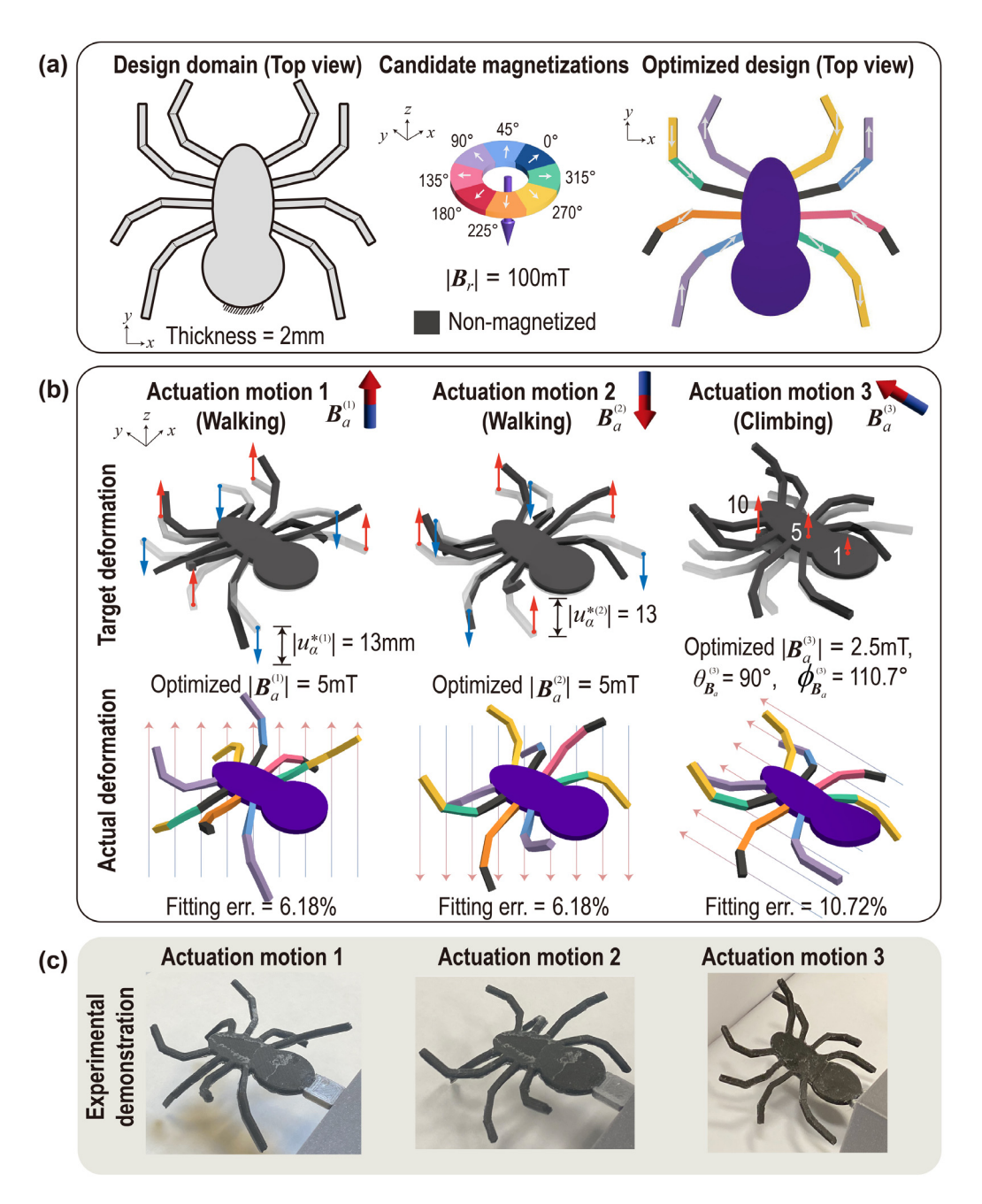


Fig. 5. Spider-inspired shape programming robot with "walking" and "climbing" modes: (a) Design domain, candidate magnetization vectors, and optimized magnetization distribution; (b) Target and actual motions under the optimized magnetic actuation; (c) Experimental demonstration for the three actuation motions.

4.3. Magneto-active actuators with maximized actuation performance

In this example, we aim to discover magneto-active actuators with maximized actuated displacements by optimizing both their geometries and magnetization distributions simultaneously. We consider the design domain of a

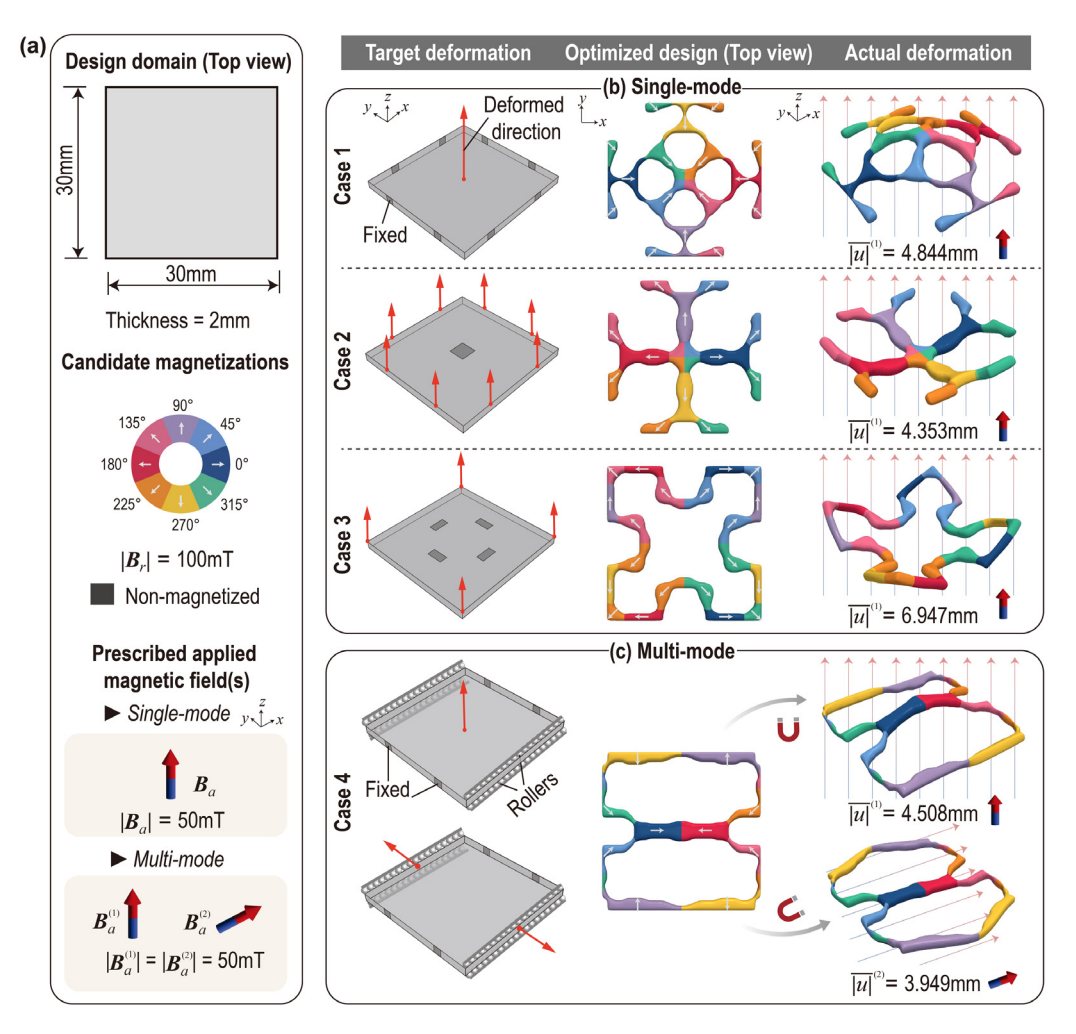


Fig. 6. Magneto-active actuators: (a) Design domain, candidate magnetization vectors, and prescribed applied magnetic fields; (b) Single-mode target deformation, optimized magnetization distribution, and actual deformations under magnetic actuation; (c) Multi-mode target deformations, optimized magnetization distribution, and actual deformations under magnetic actuation.

square sheet with dimensions of $30 \text{ mm} \times 30 \text{ mm} \times 2 \text{ mm}$ (see Fig. 6(a)) and discretize it using $120 \times 120 \times 4 = 57,600$ 8-node hexahedral finite elements. To model the feedback force of the actuator, we assign springs to the control DOFs with constant stiffness values k_{out} . The objective function $f_2(\cdot)$ (Eq. (19)) is used to maximize the actuated displacements at the control DOFs. This example considers two scenarios: (1) optimization of a single-mode actuator, which produces one unique out-of-plane deformation mode, and (2) optimization of a multi-mode actuator, which produces both in-plane and out-of-plane deformations under different applied magnetic fields. In both scenarios, the nonlinear elastic behavior of the material is modeled by a compressible LP model with parameters $\alpha_1 = 1.1913$, $\alpha_2 = -1.8503$, $\mu_1 = 0.0359$ MPa, and $\mu_2 = 0.0038$ MPa (the shear modulus is $\mu = 0.0397$ MPa). The Poisson's ratio is set as $\nu = 0.49$. A total of $N_m = 8$ candidate magnetization vectors are distributed in the x-y plane with 45° separation, with a magnitude of 100 mT. The initial guesses of the density and magnetization distribution for each finite element are set as $\rho_e = v_{\text{max}} = 0.3$ and $\xi_e^{(j)} = 1/N_m$, $j = 1, \dots, 8$, respectively. The filter radii (Eq. (9)) for both density and magnetization design variables are set as $R_\rho = R_m = 2$ mm. The stress constraint is applied to reduce thin members and hinge-like connections with a p-norm factor of $p_n = 16$.

4.3.1. Single-mode magneto-active actuators

In this subsection, we consider three design cases with different out-of-plane deformation modes. The boundary conditions and the corresponding target actuation modes are shown in Fig. 6(b) Cases 1–3. For all the cases, the

applied magnetic field B_a is prescribed as perpendicular to the design domain with a magnitude of 50 mT. The springs are connected to the control DOFs in the thickness direction with $k_{\text{out}} = 0.002$ N/mm for Case 1 and $k_{\text{out}} = 0.003$ N/mm for Case 2 and Case 3. Based on our numerical experience, the stress limit is set as $\sigma_{\text{max}} = 1$ MPa for Case 1 and $\sigma_{\text{max}} = 0.04$ MPa for Case 2 and Case 3. The maximized actuation performance is evaluated by the average of the absolute value of displacements at the control DOFs, which is given by

$$\overline{|u|}^{(\ell)} = \frac{1}{N_{\alpha}^{(\ell)}} \sum_{\alpha=1}^{N_{\alpha}^{(\ell)}} |u_{\alpha}^{(\ell)}|, \quad \ell = 1, \dots, N_{\ell}.$$

$$(21)$$

Fig. 6(b) shows the optimized single-mode designs and their deformation configurations. In Case 1, the magnetization directions of all the members are pointing toward the center control point. Under the applied magnetic field, the magnetized members are actuated to align with the direction of the applied field through magnetic torque and bending, resulting in an upward movement of the center part with a displacement of $\overline{|u|}^{(1)} = 4.844$ mm. The magnetization direction and the orientation of the members tend to be the same, which is an efficient way to maximize the output actuation displacement. In Case 2, the design domain is fixed at the center, and 8 control DOFs are considered. The optimized design shows that every control DOF is connected to the boundary via members whose orientation is parallel to the embedded magnetization direction, leading to a displacement of $\overline{|u|}^{(1)} = 4.353$ mm. In Case 3, the design domain is fixed at the bottom at 4 different locations in the center. The control DOFs are prescribed at the four corners of the design domain. The optimized design shows a similar trend where the control DOFs are connected to the boundaries with the magnetization distributed along the member directions. Actuated by magnetic torque and member bending, the output displacement is $\overline{|u|}^{(1)} = 6.947$ mm. From the generated actuator designs, we find that the out-of-plane deformation is mainly due to the bending of members induced by local magnetic torque. To maximize the out-of-plane actuation performance, it is effective to align the magnetization directions with the member orientations.

4.3.2. Multi-functional magneto-active actuators

In this subsection, we aim to design multi-functional magneto-active actuators that can achieve both in-plane and out-of-plane target actuation modes under different applied magnetic fields $B_a^{(\ell)}$, $\ell=1,\ldots,N_l$ ($N_l=2$). The boundary conditions and the two actuation modes are shown in Fig. 6(c) Case 4. In the first actuation mode, the out-of-plane deformation of the central point is maximized under the applied magnetic field $B_a^{(1)}$ pointing upward (in the positive z-direction) with a magnitude of 50 mT. A spring is attached to the control DOF in the out-of-plane direction with a stiffness of $k_{\text{out}}=0.002$ N/mm. In the second actuation mode, we assign the control DOFs at the central layer of the design domain. The displacements along the y-direction are controlled to generate maximized expansion. The stiffness of the attached springs is $k_{\text{out}}=0.002$ N/mm. The external magnetic field $B_a^{(2)}$ is applied along the positive x-direction with a magnitude of 50 mT. It is important to note that we restrict the displacement in the z-direction by assigning rollers on the edge boundaries along the x-direction to prevent unexpected out-of-plane deformations in the first actuation mode. The stress upper bound is set as $\sigma_{\text{max}}=0.04$ MPa.

In Fig. 6(c), we show the optimized design and the deformation modes under the corresponding applied magnetic fields. It can be observed that the magnetization directions of the four inclined inner members and the central horizontal member point toward the central control point. Similar to the actuation mechanism in Section 4.3.1, under the out-of-plane magnetic field $B_a^{(1)}$, these members bend in the z-direction driven by the magnetic torque, resulting in an out-of-plane deformation of $\overline{|u|}^{(1)} = 4.508$ mm at the central control DOF. For the in-plane actuation mode, the magnetization directions of the two pairs of horizontal members at the top and bottom sides are perpendicular to the applied in-plane magnetic field $B_a^{(2)}$. Under $B_a^{(2)}$, these members bend to align the magnetization direction with the applied magnetic field direction, pushing the actuator to deform in the target expansion mode with $\overline{|u|}^{(2)} = 3.949$ mm, similar to the actuation mechanism of in-plane designs reported in [4]. The magnetized members contributing to the out-of-plane and in-plane deformation modes are somewhat separated, but all make use of the bending mechanism. Due to the remote and wireless actuation strategy, this multi-mode actuator design has great potential for biomedical applications such as drug delivery and minimally invasive interventions [58–60].

To validate our numerical results, we fabricate and conduct experiments on the optimized multi-functional actuator as shown in Fig. 7(a). The fabrication process and experimental setup are detailed in Appendix C. The boundary condition is the same as the numerical design shown in Fig. 6(c) Case 4. The magnitudes of the applied

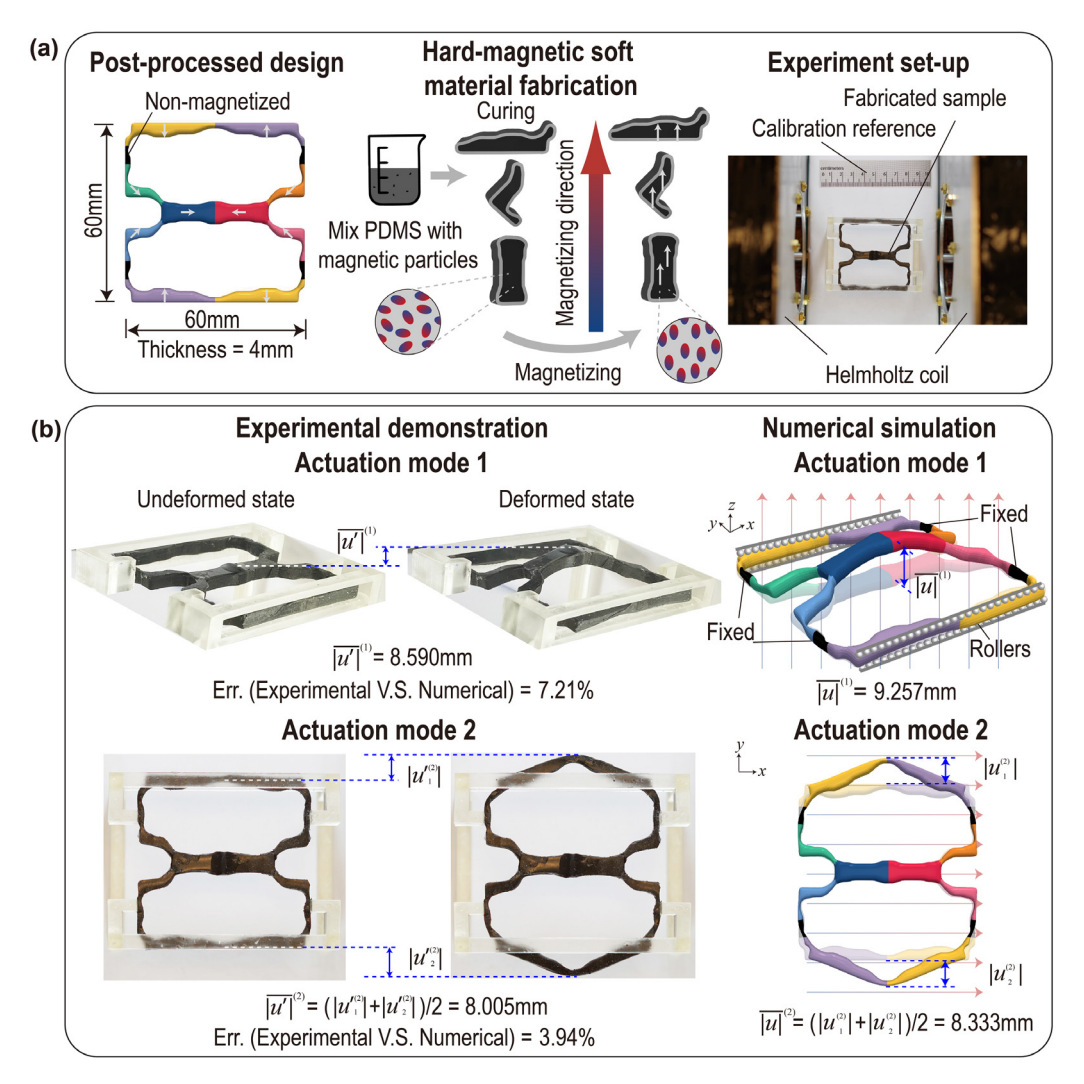


Fig. 7. Experimental validation of optimized multi-functional magneto-active actuator: (a) Post-processed numerical design; Hard-magnetic soft material fabrication; Experiment set-up; (b) Validation of experimental demonstration and numerical simulation.

external magnetic fields are $|B_a^{(1)}| = |B_a^{(2)}| = 50$ mT. To ease the manufacturing difficulty, the magnetization of the design is post-processed as shown in Fig. 7(a), and the dimension is scaled up to 60 mm × 60mm × 4 mm. The material parameters we adopted for the numerical simulation are determined from experimental material characterization (see Appendix B). As shown in Fig. 7(b), when the applied magnetic field $B_a^{(1)}$ is in the positive z-direction, the central point deforms upward due to the bending of the surrounding members. When the applied magnetic field is switched to $B_a^{(2)}$ in the positive x-direction, the manufactured design demonstrates an expansion mode, which is in good agreement with the finite element prediction. To evaluate the accuracy of the experimental validation, we define the comparison error as

Experimental error =
$$\left| \frac{\overline{|u'|}^{(\ell)} - \overline{|u|}^{(\ell)}}{\overline{|u|}^{(\ell)}} \right|$$
, (22)

where u' represents the experimentally measured displacement. According to Eq. (22), the experimental errors for actuation mode 1 and mode 2 are quantified as 7.21% and 3.94%, respectively. The experimental validation shows that the programmed 3D magneto-responsive deformations can be physically realized with high accuracy.

5. Conclusions

This paper presents a topology optimization framework for the inverse design of magneto-active metasurfaces and robots which realize complex target shapes, deformation modes, and actuated responses in 3D space. To ensure maximal design freedom and programming precision, we propose novel schemes to parameterize the full design space of topology, remnant magnetization distribution, and external magnetic field. Specifically, the topology is designed to program the stiffness distribution, while the magnetization and applied magnetic field are designed to distribute the magnetic torque over the structures. By simultaneously optimizing all three design variables, the structure's programmability is significantly improved. Additionally, we present a scheme for interpolating the Helmholtz free energy function from the three sets of design variables, which together contribute to the nonlinear mechanical response of the design. Three design examples are presented to demonstrate the effectiveness and ability of the proposed topology optimization framework to generate designs that can achieve various complex 3D target deformations with high precision. The first example designs the Kirigami metasurfaces to achieve different prescribed out-of-plane deformations by optimizing the magnetization distributions under different prescribed magnetic fields. The second example generates spider-inspired soft robots by optimizing the magnetization distribution and the applied magnetic fields simultaneously. The optimized robots are able to achieve different locomotion modes, including "swimming", "steering", "walking", and "climbing", under varying optimized external magnetic fields. The last example explores magneto-active actuators with target and maximized deformation modes by optimizing both topology and magnetization distributions. The optimized designs are capable of achieving both programmable out-of-plane and in-plane deformations under different magnetic fields. Furthermore, two representative designs are fabricated via a hybrid manufacturing approach and experimentally tested to validate that the programmed 3D deformations can be physically achieved with an error of less than 8%. We envision that the proposed framework could lead to the design of magneto-active metasurfaces for various applications, such as biomedical devices [58–60] and energy harvesting devices [61.62].

While the current results are promising, there is substantial scope for improvement in future studies. From the modeling perspective, adopting a more accurate and fully-coupled magneto-mechanical model [27,29,30] that is capable of: (1) considering the coupling of magnetic particle interactions [27], (2) solving the magnetic field from Maxwell equation instead of prescribing it, and (3) modeling the heterogeneous and non-uniform external magnetic field [63,64] are important directions of our future work. Developing analytical methods for designing magneto-active soft materials is also an important direction to explore [65]. Moreover, to minimize the influence of the deformation induced by the magnetic interaction between adjacent members, we could formulate constraints to avoid the formation of opposite magnetization directions in close regions that may cause severe self-interaction and include constraints to restrain the level of deformation in the absence of an actuating magnetic field. To expand the design space and enhance programmability in magneto-active designs, another direction is to develop advanced parameterization schemes allowing for continuous variation of remnant magnetization distributions. The designs can be further improved by considering manufacturing constraints [55] or buckling constraints [66,67] to improve the manufacturability and stability, respectively. Finally, we plan to explore different manufacturing methods for fabricating optimized hard-magnetic soft materials with more complex geometries and magnetization distributions.

Declaration of competing interest

The authors declare that they have no known competing financial interests or personal relationships that could have appeared to influence the work reported in this paper.

Data availability

Data will be made available on request.

Acknowledgments

The authors acknowledge the financial support from the U.S. Defense Advanced Research Projects Agency (DARPA) Young Faculty Award (N660012314013) and the U.S. National Science Foundation (NSF) CAREER Award CMMI-2047692. The information provided in this paper is the sole opinion of the authors and does not necessarily reflect the view of the sponsoring agency. The authors acknowledge the use of facilities and instrumentation at the Materials Research Laboratory Central Research Facilities, University of Illinois, partially supported by U.S. National Science Foundation (NSF) through the University of Illinois Materials Research Science and Engineering Center DMR-1720633.

Appendix A. Sensitivity analysis

We solve the optimization problem Eq. (17) using the gradient-based algorithm. The sensitivities (gradients) of the objective and constraint functions with respect to the design variables are calculated using the adjoint method [9] and chain rule. Assuming a general function J that can represent objective or constraint functions, gradients with respect to the design variables of the density ρ , magnetization ξ , and the applied magnetic field $A_{B_a}^{(\ell)}$, $\phi_{B_a}^{(\ell)}$, and $\theta_{B_a}^{(\ell)}$ are given by

$$\frac{\partial J}{\partial \rho_e} = \sum_{i \in \mathscr{I}_r(R_o)} \left(\frac{\partial J}{\partial \bar{\rho}_i} \frac{\partial \bar{\rho}_i}{\partial \bar{\rho}_i} \frac{\partial \bar{\rho}_i}{\partial \rho_e} \right),\tag{A.1}$$

$$\frac{\partial J}{\partial \xi_e^{(k)}} = \sum_{i \in \mathscr{I}_e(R_m)} \left(\sum_{j=1}^{N_m} \left(\frac{\partial J}{\partial \overline{m}_i^{(j)}} \frac{\partial \overline{m}_i^{(j)}}{\partial \bar{\xi}_i^{(k)}} \right) \frac{\partial \bar{\xi}_i^{(k)}}{\partial \bar{\xi}_i^{(k)}} \frac{\partial \tilde{\xi}_i^{(k)}}{\partial \xi_e^{(k)}} \right), \tag{A.2}$$

$$\frac{\partial J}{\partial A_{B_a}^{(\ell)}} = \frac{\partial J}{\partial \mathbf{B}_a^{(\ell)}} \frac{\partial \mathbf{B}_a^{(\ell)}}{\partial A_{B_a}^{(\ell)}},\tag{A.3}$$

$$\frac{\partial J}{\partial \phi_{B_a}^{(\ell)}} = \frac{\partial J}{\partial \mathbf{B}_a^{(\ell)}} \frac{\partial \mathbf{B}_a^{(\ell)}}{\partial \phi_{B_a}^{(\ell)}},\tag{A.4}$$

and

$$\frac{\partial J}{\partial \theta_{B_a}^{(\ell)}} = \frac{\partial J}{\partial \mathbf{B}_a^{(\ell)}} \frac{\partial \mathbf{B}_a^{(\ell)}}{\partial \theta_{B_a}^{(\ell)}},\tag{A.5}$$

where $j = 1, ..., N_m$ and $l = 1, ..., N_\ell$.

The derivatives of $\partial \bar{\rho}_i / \partial \tilde{\rho}_i$ and $\partial \tilde{\rho}_i / \partial \rho_e$ are given as

$$\frac{\partial \bar{\rho}_i}{\partial \tilde{\rho}_i} = \frac{\beta_\rho \left(\tanh \left(\beta_\rho \left(\tilde{\rho}_i - \frac{1}{2} \right) \right)^2 - 1 \right)}{\tanh \left(-\frac{\beta_\rho}{2} \right) - \tanh \left(\frac{\beta_\rho}{2} \right)} \tag{A.6}$$

and

$$\frac{\partial \tilde{\rho}_i}{\partial \rho_e} = \frac{w_e v_e}{\sum_{h \in \mathscr{I}_e(R_\rho)} w_h v_h}.$$
(A.7)

The derivatives of $\partial \overline{m}_i^{(j)}/\partial \overline{\xi}_i^{(k)}$, $\partial \overline{\xi}_i^{(k)}/\partial \widetilde{\xi}_i^{(k)}$, and $\partial \widetilde{\xi}_i^{(k)}/\partial \xi_e^{(k)}$ are given as

$$\frac{\partial \overline{m}_{i}^{(j)}}{\partial \bar{\xi}_{i}^{(k)}} = \sum_{i=1}^{2^{N_{m}}} s_{i}^{(j)} \left\{ (-1)^{\left(N_{m} + \sum_{j=1}^{N_{m}} c_{i}^{(j)}\right)} \prod_{\substack{t=1\\t \neq k}}^{N_{m}} \left(\bar{\xi}_{i}^{(t)} + c_{i}^{(t)} - 1\right) \right\}, \tag{A.8}$$

$$\frac{\partial \bar{\xi}_{i}^{(k)}}{\partial \tilde{\xi}_{i}^{(k)}} = \frac{\beta_{m} \left(\tanh \left(\beta_{m} \left(\tilde{\xi}_{i}^{(k)} - \frac{1}{2} \right) \right)^{2} - 1 \right)}{\tanh \left(-\frac{\beta_{m}}{2} \right) - \tanh \left(\frac{\beta_{m}}{2} \right)},\tag{A.9}$$

and

$$\frac{\partial \tilde{\xi}_i^{(k)}}{\partial \xi_e^{(k)}} = \frac{w_i v_i}{\sum_{h \in \mathcal{J}_e(R_m)} w_h v_h}.$$
(A.10)

The derivatives of $\partial \boldsymbol{B}_{a}^{(\ell)}/\partial A_{B_{a}}^{(\ell)}$, $\partial \boldsymbol{B}_{a}^{(\ell)}/\partial \phi_{B_{a}}^{(\ell)}$, and $\partial \boldsymbol{B}_{a}^{(\ell)}/\partial \theta_{B_{a}}^{(\ell)}$ are given as

$$\frac{\partial \boldsymbol{B}_{a}^{(\ell)}}{\partial A_{B_{a}}^{(\ell)}} = \begin{bmatrix}
\sin\left(\phi_{B_{a}}^{(\ell)}\right)\cos\left(\theta_{B_{a}}^{(\ell)}\right) \\
\sin\left(\phi_{B_{a}}^{(\ell)}\right)\sin\left(\theta_{B_{a}}^{(\ell)}\right) \\
\cos\left(\phi_{B_{a}}^{(\ell)}\right)
\end{bmatrix}, \tag{A.11}$$

$$\frac{\partial \boldsymbol{B}_{a}^{(\ell)}}{\partial \boldsymbol{\phi}_{B_{a}}^{(\ell)}} = \begin{bmatrix}
A_{B_{a}}^{(\ell)} \cos \left(\boldsymbol{\phi}_{B_{a}}^{(\ell)}\right) \cos \left(\boldsymbol{\theta}_{B_{a}}^{(\ell)}\right) \\
A_{B_{a}}^{(\ell)} \cos \left(\boldsymbol{\phi}_{B_{a}}^{(\ell)}\right) \sin \left(\boldsymbol{\theta}_{B_{a}}^{(\ell)}\right) \\
-A_{B_{a}}^{(\ell)} \sin \left(\boldsymbol{\phi}_{B_{a}}^{(\ell)}\right)
\end{bmatrix}, \tag{A.12}$$

and

$$\frac{\partial \boldsymbol{B}_{a}^{(\ell)}}{\partial \theta_{B_{a}}^{(\ell)}} = \begin{bmatrix} -A_{B_{a}}^{(\ell)} \sin\left(\phi_{B_{a}}^{(\ell)}\right) \sin\left(\theta_{B_{a}}^{(\ell)}\right) \\ A_{B_{a}}^{(\ell)} \sin\left(\phi_{B_{a}}^{(\ell)}\right) \cos\left(\theta_{B_{a}}^{(\ell)}\right) \\ 0 \end{bmatrix}. \tag{A.13}$$

The sensitivities with respect to the physical density, magnetization and applied magnetic field variables $\overline{\rho}$, $\overline{m}^{(j)}$, and $B_a^{(\ell)}$ are calculated by

$$\frac{\partial J}{\partial \overline{\rho}_{e}} = \frac{\partial J\left(\overline{\rho}, \overline{\boldsymbol{m}}^{(1)}, \dots, \overline{\boldsymbol{m}}^{(N_{m})}, \boldsymbol{B}_{a}^{(\ell)}, \boldsymbol{u}^{(\ell)}\right)}{\partial \overline{\rho}_{e}} + (\boldsymbol{\lambda}^{(\ell)})^{T} \frac{\partial \mathbf{R}\left(\overline{\rho}, \overline{\boldsymbol{m}}^{(1)}, \dots, \overline{\boldsymbol{m}}^{(N_{m})}, \boldsymbol{B}_{a}^{(\ell)}, \boldsymbol{u}^{(\ell)}\right)}{\partial \overline{\rho}_{e}}, \tag{A.14}$$

$$\frac{\partial J}{\partial \overline{m}_{e}^{(j)}} = \frac{\partial J\left(\overline{\rho}, \overline{m}^{(1)}, \dots, \overline{m}^{(N_{m})}, \boldsymbol{B}_{a}^{(\ell)}, \boldsymbol{u}^{(\ell)}\right)}{\partial \overline{m}_{e}^{(j)}} + (\boldsymbol{\lambda}^{(\ell)})^{T} \frac{\partial \mathbf{R}\left(\overline{\rho}, \overline{m}^{(1)}, \dots, \overline{m}^{(N_{m})}, \boldsymbol{B}_{a}^{(\ell)}, \boldsymbol{u}^{(\ell)}\right)}{\partial \overline{m}_{e}^{(j)}}, \tag{A.15}$$

and

$$\frac{\partial J}{\partial \boldsymbol{B}_{a}^{(\ell)}} = \frac{\partial J\left(\overline{\boldsymbol{\rho}}, \overline{\boldsymbol{m}}^{(1)}, \dots, \overline{\boldsymbol{m}}^{(N_{m})}, \boldsymbol{B}_{a}^{(\ell)}, \boldsymbol{u}^{(\ell)}\right)}{\partial \boldsymbol{B}_{a}^{(\ell)}} + (\boldsymbol{\lambda}^{(\ell)})^{T} \frac{\partial \mathbf{R}\left(\overline{\boldsymbol{\rho}}, \overline{\boldsymbol{m}}^{(1)}, \dots, \overline{\boldsymbol{m}}^{(N_{m})}, \boldsymbol{B}_{a}^{(\ell)}, \boldsymbol{u}^{(\ell)}\right)}{\partial \boldsymbol{B}_{a}^{(\ell)}}, \tag{A.16}$$

where $\lambda^{(\ell)}$ is the adjoint vector solved by the following adjoint system

$$\left[\boldsymbol{K}_{T}^{(\ell)}(\overline{\boldsymbol{\rho}}, \overline{\boldsymbol{m}}^{(1)}, \dots, \overline{\boldsymbol{m}}^{(N_{m})}, \boldsymbol{B}_{a}^{(\ell)}, \boldsymbol{u}^{(\ell)})\right] \boldsymbol{\lambda}^{(\ell)} = -\frac{\partial J\left(\overline{\boldsymbol{\rho}}, \overline{\boldsymbol{m}}^{(1)}, \dots, \overline{\boldsymbol{m}}^{(N_{m})}, \boldsymbol{B}_{a}^{(\ell)}, \boldsymbol{u}^{(\ell)}\right)}{\partial \boldsymbol{u}^{(\ell)}}, \tag{A.17}$$

with $\pmb{K}_T^{(\ell)} \doteq \partial \mathbf{R}/\partial \pmb{u}^{(l)}$ being the tangent stiffness matrix associated with the lth magnetic field $\pmb{B}_a^{(\ell)}$ when $\pmb{u}^{(l)}$ is solved in the equilibrium equation. The expressions of $\partial \mathbf{R}/\partial \overline{\rho}_e$, $\partial \mathbf{R}/\partial \overline{m}_e^{(j)}$, and $\partial \mathbf{R}/\partial \pmb{B}_a^{(\ell)}$ are given as

$$\frac{\partial \mathbf{R}}{\partial \overline{\rho}_{e}} = \mathbf{A} \int_{O_{e}} \mathbf{B}^{\mathsf{T}} \left(\frac{\partial}{\partial \mathbf{F}} \left(\frac{\partial W_{e}}{\partial \overline{\rho}_{e}} \right) \right)^{V} dX, \tag{A.18}$$

$$\frac{\partial \mathbf{R}}{\partial \overline{m}_{s}^{(j)}} = \mathbf{A} \int_{\Omega_{e}} \mathbf{B}^{\mathsf{T}} \left(\frac{\partial}{\partial F} \left(\frac{\partial W_{e}}{\partial \overline{m}_{s}^{(j)}} \right) \right)^{V} dX, \tag{A.19}$$

and

$$\frac{\partial \mathbf{R}}{\partial \boldsymbol{B}_{a}^{(\ell)}} = \mathbf{A}_{e=1}^{N_e} \int_{\Omega_e} \mathbf{B}^{\mathsf{T}} \left(\frac{\partial}{\partial \boldsymbol{F}} \left(\frac{\partial W_e}{\partial \boldsymbol{B}_{a}^{(\ell)}} \right) \right)^V dX, \tag{A.20}$$

where V represents the voigt notation, \mathbf{B} is the strain-displacement matrix and W_e is given in Eq. (14). For brevity, the explicit expressions for $\partial W_e/\partial\overline{\rho}_e$, $\partial W_e/\partial\overline{m}_e^{(j)}$, and $\partial W_e/\partial \boldsymbol{B}_a^{(\ell)}$ are not provided here. The first terms in Eqs. (A.14)-(A.16) and $\partial J\left(\overline{\rho},\overline{m}^{(1)},\ldots,\overline{m}^{(N_m)},\boldsymbol{B}_a^{(\ell)},\boldsymbol{u}^{(\ell)}\right)/\partial\boldsymbol{u}^{(\ell)}$ in Eq. (A.17) are determined

The first terms in Eqs. (A.14)–(A.16) and $\partial J\left(\overline{\rho}, \overline{\boldsymbol{m}}^{(1)}, \ldots, \overline{\boldsymbol{m}}^{(N_m)}, \boldsymbol{B}_a^{(\ell)}, \boldsymbol{u}^{(\ell)}\right)/\partial \boldsymbol{u}^{(\ell)}$ in Eq. (A.17) are determined by the specific form of the general function J. For example, with respect to the objective function in Eq. (18), these four terms are given as

$$\frac{\partial f_1\left(\boldsymbol{u}^{(1)},\ldots,\boldsymbol{u}^{(N_\ell)}\right)}{\partial \overline{\rho}_e} = 0,$$

$$\frac{\partial f_1\left(\boldsymbol{u}^{(1)},\ldots,\boldsymbol{u}^{(N_\ell)}\right)}{\partial \overline{m}_e^{(j)}} = 0,$$
and
$$\frac{\partial f_1\left(\boldsymbol{u}^{(1)},\ldots,\boldsymbol{u}^{(N_\ell)}\right)}{\partial \boldsymbol{u}^{(\ell)}} = \frac{2}{N_\alpha^{(k)}} \left(\frac{u_\alpha^{(k)} - u_\alpha^{*(k)}}{u_\alpha^{*(k)}}\right)$$
with $\ell = 1,\ldots,N_\ell$, $k = \operatorname{argmax}\left(f_1\left(\boldsymbol{u}^{(1)},\ldots,\boldsymbol{u}^{(N_\ell)}\right)\right)$.

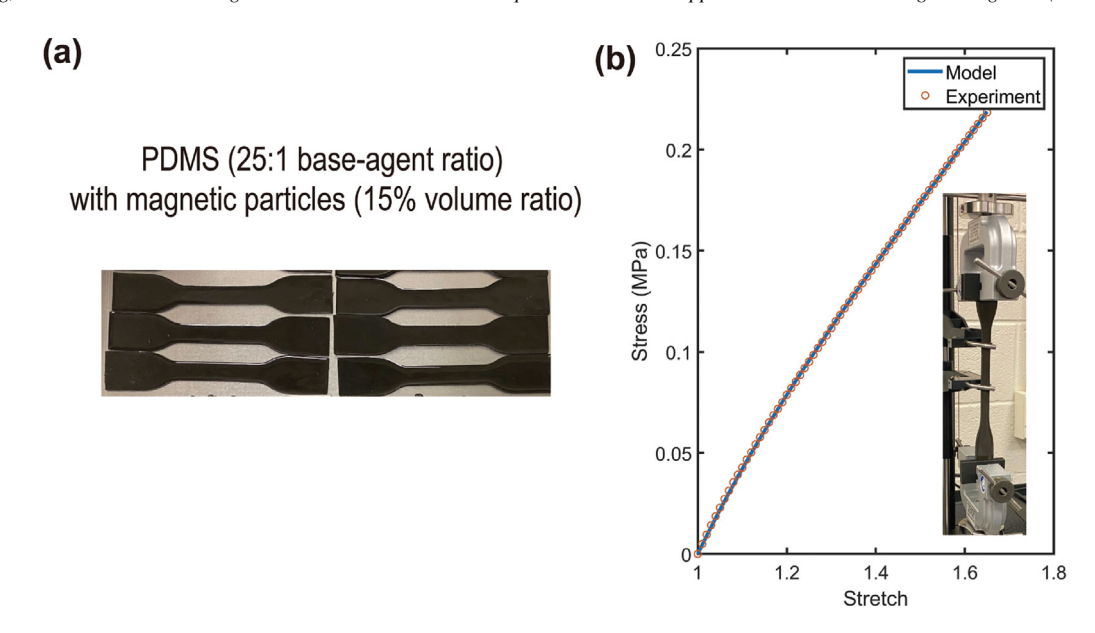


Fig. B.8. Uniaxial tension test of hard-magnetic soft materials: (a) Fabricated hard-magnetic soft material dog-bone samples; (b) Comparisons of the measured uniaxial stress-stretch response and the corresponding predictions by the LP hyperelastic model.

Appendix B. Material characterization of mechanical properties of hard-magnetic soft materials

The hard-magnetic soft material is fabricated by mixing polydimethylsiloxane (PDMS) elastomer according to a certain base-agent ratio with embedded neodymium–iron–boron (NdFeB, Magnequench, Singapore) microparticles by hand stirring for 20 min. The mixture is degassed under a -80.0 kPa atmosphere for 60 min for bubble removal. Dog-bone samples are fabricated through a mold casting process for the uniaxial tension test. Specifically, the liquid mixture is poured into 3D-printed Polyvinyl Alcohol (PVA) mold and cured at 175° F for 120 min. The sample dimensions are determined according to ASTM D412-16. A total of 6 dog-bone samples are tested for the hard-magnetic soft material made of PDMS with 25:1 base-agent ratio and embedded magnetic particles of 15% volume ratio. All samples are tested on a loading machine (Instron 68TM-30) using a 500 N load cell with a 5.0 mm/min overhead speed.

The characterization of the hard-magnetic soft material is based on the uniaxial tension test. The uniaxial tension test data are demonstrated in Fig. B.8. The tested nominal stress–stretch curve is fitted using the isotropic, compressible Lopez-Pamies (LP) hyperelastic model (Eq. (2)). This study uses a two-term model, i.e., n=2. Based on least-square fit, the four material parameters are obtained as $\alpha_1=1.4121$, $\alpha_2=1.3368$, $\mu_1=0.0772$ MPa, and $\mu_2=0.0771$ MPa.

Appendix C. Fabrication of the optimized design and experiment setup

The optimized designs are obtained through a mold casting process. We divide the optimized geometries into several components according to the magnetization direction (Fig. 7(a)). The geometries of different components are then input used to generate the STL files ready for 3D printing. The molds are then 3D printed using fused deposition modeling printers (Original Prusa i3 MK3S+ 3D printer) with Polyvinyl Alcohol (PVA) filament. The hard-magnetic soft material is made by mixing the PDMS (the base-agent ratios are 10:1 and 25:1 in Sections 4.2.2 and 4.3.2, respectively) with embedded magnetic particles of 15% volume ratio. The liquid mixture is then poured into the 3D-printed molds after degassing and cured at 175° F for 120 min. After curing and demolding, the modular components are magnetized to the desired magnetization direction by an impulse magnetic field at 2T using an impulse magnetizer. To guarantee the accuracy of the remnant magnetization direction, we utilize 3D-printed PLA guides that ensure the proper placement of the structural components within the magnetizer. The remnant magnetic flux density of the cured hard-magnetic soft material is measured as 100 mT using a Quantum Design MPMS3 SQUID Magnetometer. The integrated optimized designs are assembled by bonding separate components at the

interface using the Sil-poxy adhesive (Smooth-On Inc., USA). 3D-printed support frames are fabricated to fix the designs. In Section 4.2.2, the support is made of Polylactic Acid (PLA) printed via a fused deposition modeling printer. In Section 4.3.2, the support is made of translucent Acrylonitrile Butadiene Styrene (ABS) resin using a stereolithography 3D printer (Elegoo Saturn S). The external magnetic fields are generated by a pair of Helmholtz coils and measured using a magnetic meter to ensure the metasurfaces and robots are positioned within a range of nearly uniform magnetic field.

Appendix D. Supplementary data

Supplementary material related to this article can be found online at https://doi.org/10.1016/j.cma.2023.116065.

References

- [1] A. Nojoomi, J. Jeon, K. Yum, 2D material programming for 3D shaping, Nature Commun. 12 (1) (2021) 1-8.
- [2] Y. Kim, H. Yuk, R. Zhao, S.A. Chester, X. Zhao, Printing ferromagnetic domains for untethered fast-transforming soft materials, Nature 558 (7709) (2018) 274–279.
- [3] R. Zhao, Y. Kim, S.A. Chester, P. Sharma, X. Zhao, Mechanics of hard-magnetic soft materials, J. Mech. Phys. Solids 124 (2019) 244–263.
- [4] Z. Zhao, X.S. Zhang, Topology optimization of hard-magnetic soft materials, J. Mech. Phys. Solids 158 (2022) 104628.
- [5] P. Lloyd, A.K. Hoshiar, T. da Veiga, A. Attanasio, N. Marahrens, J.H. Chandler, P. Valdastri, A learnt approach for the design of magnetically actuated shape forming soft tentacle robots, IEEE Robot. Autom. Lett. 5 (3) (2020) 3937–3944.
- [6] C. Ma, Y. Chang, S. Wu, R.R. Zhao, Deep learning-accelerated designs of tunable magneto-mechanical metamaterials, ACS Appl. Mater. Interfaces 14 (29) (2022) 33892–33902.
- [7] S. Wu, C.M. Hamel, Q. Ze, F. Yang, H.J. Qi, R. Zhao, Evolutionary algorithm-guided voxel-encoding printing of functional hard-magnetic soft active materials, Adv. Intell. Syst. 2 (8) (2020) 2000060.
- [8] L. Wang, D. Zheng, P. Harker, A.B. Patel, C.F. Guo, X. Zhao, Evolutionary design of magnetic soft continuum robots, Proc. Natl. Acad. Sci. 118 (21) (2021).
- [9] M.P. Bendsoe, O. Sigmund, Topology Optimization: Theory, Methods, and Applications, Springer Science & Business Media, 2013.
- [10] C. Wang, Z. Zhao, M. Zhou, O. Sigmund, X.S. Zhang, A comprehensive review of educational articles on structural and multidisciplinary optimization, Struct. Multidiscip. Optim. 64 (5) (2021) 2827–2880.
- [11] P.W. Christensen, A. Klarbring, An Introduction to Structural Optimization, Vol. 153, Springer Science & Business Media, 2008.
- [12] Q. Li, O. Sigmund, J.S. Jensen, N. Aage, Reduced-order methods for dynamic problems in topology optimization: A comparative study, Comput. Methods Appl. Mech. Engrg. 387 (2021) 114149.
- [13] G.A. da Silva, A.T. Beck, O. Sigmund, Structural topology optimization with predetermined breaking points, Comput. Methods Appl. Mech. Engrg. 400 (2022) 115610.
- [14] E. Garner, J. Wu, A.A. Zadpoor, Multi-objective design optimization of 3D micro-architected implants, Comput. Methods Appl. Mech. Engrg. 396 (2022) 115102.
- [15] M. Xiao, X. Liu, Y. Zhang, L. Gao, J. Gao, S. Chu, Design of graded lattice sandwich structures by multiscale topology optimization, Comput. Methods Appl. Mech. Engrg. 384 (2021) 113949.
- [16] G.H. Yoon, A new monolithic design approach for topology optimization for transient fluid-structure interaction system, Comput. Methods Appl. Mech. Engrg. 403 (2023) 115729.
- [17] L. Chen, H. Lian, S. Natarajan, W. Zhao, X. Chen, S. Bordas, Multi-frequency acoustic topology optimization of sound-absorption materials with isogeometric boundary element methods accelerated by frequency-decoupling and model order reduction techniques, Comput. Methods Appl. Mech. Engrg. 395 (2022) 114997.
- [18] Y. Noguchi, T. Yamada, Topology optimization for acoustic structures considering viscous and thermal boundary layers using a sequential linearized Navier–Stokes model, Comput. Methods Appl. Mech. Engrg. 394 (2022) 114863.
- [19] L. Alacoque, R.T. Watkins, A.Y. Tamijani, Stress-based and robust topology optimization for thermoelastic multi-material periodic microstructures, Comput. Methods Appl. Mech. Engrg. 379 (2021) 113749.
- [20] X. Xu, X.D. Gu, S. Chen, Shape and topology optimization of conformal thermal control structures on free-form surfaces: A dimension reduction level set method (DR-LSM), Comput. Methods Appl. Mech. Engrg. 398 (2022) 115183.
- [21] W. Zhang, X. Yan, Y. Meng, C. Zhang, S.-K. Youn, X. Guo, Flexoelectric nanostructure design using explicit topology optimization, Comput. Methods Appl. Mech. Engrg. 394 (2022) 114943.
- [22] R. Ortigosa, J. Martínez-Frutos, A. Gil, A computational framework for topology optimisation of flexoelectricity at finite strains considering a multi-field micromorphic approach, Comput. Methods Appl. Mech. Engrg. 401 (2022) 115604.
- [23] J. Tian, M. Li, Z. Han, Y. Chen, X.D. Gu, Q. Ge, S. Chen, Conformal topology optimization of multi-material ferromagnetic soft active structures using an extended level set method, Comput. Methods Appl. Mech. Engrg. 389 (2022) 114394.
- [24] S. Ogawa, T. Yamada, A new design approach for thermal actuators based on topology optimization with stress constraints, Internat. J. Numer. Methods Engrg. (2022).
- [25] D. Athinarayanarao, R. Prod'hon, D. Chamoret, H.J. Qi, M. Bodaghi, J.-C. André, F. Demoly, Computational design for 4D printing of topology optimized multi-material active composites, npj Comput. Mater. 9 (1) (2023) 1–9.

- [26] R.A. Salas, A.L.F. da Silva, E.C.N. Silva, HYIMFO: Hybrid method for optimizing fiber orientation angles in laminated piezocomposite actuators, Comput. Methods Appl. Mech. Engrg. 385 (2021) 114010.
- [27] D. Mukherjee, M. Rambausek, K. Danas, An explicit dissipative model for isotropic hard magnetorheological elastomers, J. Mech. Phys. Solids 151 (2021) 104361.
- [28] D. Yan, B.F. Aymon, P.M. Reis, A reduced-order, rotation-based model for thin hard-magnetic plates, J. Mech. Phys. Solids 170 (2023) 105095.
- [29] M. Rambausek, D. Mukherjee, K. Danas, A computational framework for magnetically hard and soft viscoelastic magnetorheological elastomers, Comput. Methods Appl. Mech. Engrg. 391 (2022) 114500.
- [30] D. Mukherjee, K. Danas, A unified dual modeling framework for soft and hard magnetorheological elastomers, Int. J. Solids Struct. 257 (2022) 111513.
- [31] O. Lopez-Pamies, A new I1-based hyperelastic model for rubber elastic materials, C. R. Mec. 338 (1) (2010) 3-11.
- [32] T. Belytschko, W.K. Liu, B. Moran, K. Elkhodary, Nonlinear Finite Elements for Continua and Structures, John wiley & sons, 2014.
- [33] L. Armijo, Minimization of functions having Lipschitz continuous first partial derivatives, Pacific J. Math. 16 (1) (1966) 1-3.
- [34] X. Zhang, A.S. Ramos, G.H. Paulino, Material nonlinear topology optimization using the ground structure method with a discrete filtering scheme, Struct. Multidiscip. Optim. 55 (6) (2017) 2045–2072.
- [35] F. Ferrari, O. Sigmund, A new generation 99 line Matlab code for compliance topology optimization and its extension to 3D, Struct. Multidiscip. Optim. 62 (4) (2020) 2211–2228.
- [36] S. Engblom, D. Lukarski, Fast Matlab compatible sparse assembly on multicore computers, Parallel Comput. 56 (2016) 1-17.
- [37] F. Wang, B.S. Lazarov, O. Sigmund, On projection methods, convergence and robust formulations in topology optimization, Struct. Multidiscip. Optim. 43 (6) (2011) 767–784.
- [38] O. Sigmund, Morphology-based black and white filters for topology optimization, Struct. Multidiscip. Optim. 33 (4-5) (2007) 401-424.
- [39] Y. Zhou, T. Nomura, K. Saitou, Multi-component topology and material orientation design of composite structures (MTO-C), Comput. Methods Appl. Mech. Engrg. 342 (2018) 438–457.
- [40] X.S. Zhang, H. Chi, Z. Zhao, Topology optimization of hyperelastic structures with anisotropic fiber reinforcement under large deformations, Comput. Methods Appl. Mech. Engrg. 378 (2021) 113496.
- [41] H. Li, H. Li, L. Gao, J. Li, P. Li, Y. Yang, Topology optimization of arbitrary-shape multi-phase structure with structured meshes based on a virtual phase method, Comput. Methods Appl. Mech. Engrg. 387 (2021) 114138.
- [42] Y. Xu, Y. Gao, C. Wu, J. Fang, G. Sun, G.P. Steven, Q. Li, Machine learning based topology optimization of fiber orientation for variable stiffness composite structures, Internat. J. Numer. Methods Engrg. 122 (22) (2021) 6736–6755.
- [43] Y. Xu, Y. Gao, C. Wu, J. Fang, G. Sun, G.P. Steven, Q. Li, Concurrent optimization of topological configuration and continuous fiber path for composite structures—A unified level set approach, Comput. Methods Appl. Mech. Engrg. 399 (2022) 115350.
- [44] M.P. Bendsøe, Optimal shape design as a material distribution problem, Struct. Optim. 1 (4) (1989) 193-202.
- [45] F. Wang, B.S. Lazarov, O. Sigmund, J.S. Jensen, Interpolation scheme for fictitious domain techniques and topology optimization of finite strain elastic problems, Comput. Methods Appl. Mech. Engrg. 276 (2014) 453–472.
- [46] Y. Luo, M.Y. Wang, Z. Kang, Topology optimization of geometrically nonlinear structures based on an additive hyperelasticity technique, Comput. Methods Appl. Mech. Engrg. 286 (2015) 422–441.
- [47] R. Xue, C. Liu, W. Zhang, Y. Zhu, S. Tang, Z. Du, X. Guo, Explicit structural topology optimization under finite deformation via moving morphable void (MMV) approach, Comput. Methods Appl. Mech. Engrg. 344 (2019) 798–818.
- [48] G. Cheng, Z. Jiang, Study on topology optimization with stress constraints, Eng. Optim. 20 (2) (1992) 129-148.
- [49] G.D. Cheng, X. Guo, ε-Relaxed approach in structural topology optimization, Struct. Optim. 13 (4) (1997) 258–266.
- [50] M. Bruggi, On an alternative approach to stress constraints relaxation in topology optimization, Struct. Multidiscip. Optim. 36 (2) (2008) 125–141.
- [51] P. Duysinx, M.P. Bendsøe, Topology optimization of continuum structures with local stress constraints, Internat. J. Numer. Methods Engrg. 43 (8) (1998) 1453–1478.
- [52] K. Svanberg, The method of moving asymptotes—a new method for structural optimization, Internat. J. Numer. Methods Engrg. 24 (2) (1987) 359–373.
- [53] N. Olhoff, Multicriterion structural optimization via bound formulation and mathematical programming, Struct. Optim. 1 (1) (1989) 11–17.
- [54] X. Poulain, V. Lefevre, O. Lopez-Pamies, K. Ravi-Chandar, Damage in elastomers: nucleation and growth of cavities, micro-cracks, and macro-cracks, Int. J. Fract. 205 (1) (2017) 1–21.
- [55] S.L. Vatanabe, T.N. Lippi, C.R. de Lima, G.H. Paulino, E.C. Silva, Topology optimization with manufacturing constraints: a unified projection-based approach, Adv. Eng. Softw. 100 (2016) 97–112.
- [56] X. Kuang, S. Wu, Q. Ze, L. Yue, Y. Jin, S.M. Montgomery, F. Yang, H.J. Qi, R. Zhao, Magnetic dynamic polymers for modular assembling and reconfigurable morphing architectures, Adv. Mater. 33 (30) (2021) 2102113.
- [57] S.M. Montgomery, S. Wu, X. Kuang, C.D. Armstrong, C. Zemelka, Q. Ze, R. Zhang, R. Zhao, H.J. Qi, Magneto-mechanical metamaterials with widely tunable mechanical properties and acoustic bandgaps, Adv. Funct. Mater. 31 (3) (2021) 2005319.
- [58] A. Hong, A.J. Petruska, A. Zemmar, B.J. Nelson, Magnetic control of a flexible needle in neurosurgery, IEEE Trans. Biomed. Eng. 68 (2) (2020) 616–627.
- [59] J. Zhang, Z. Ren, W. Hu, R.H. Soon, I.C. Yasa, Z. Liu, M. Sitti, Voxelated three-dimensional miniature magnetic soft machines via multimaterial heterogeneous assembly, Science Robotics 6 (53) (2021) eabf0112.
- [60] Y. Yang, J. Wang, L. Wang, Q. Wu, L. Ling, Y. Yang, S. Ning, Y. Xie, Q. Cao, L. Li, et al., Magnetic soft robotic bladder for assisted urination, Sci. Adv. 8 (34) (2022) eabq1456.

- [61] A.H. Rahmati, R. Jia, K. Tan, X. Zhao, Q. Deng, L. Liu, P. Sharma, Theory of hard magnetic soft materials to create magnetoelectricity, Journal of the Mechanics and Physics of Solids 171 (2023) 105136.
- [62] A.H. Rahmati, R. Jia, K. Tan, L. Liu, X. Zhao, Q. Deng, P. Sharma, Giant magnetoelectricity in soft materials using hard magnetic soft materials, Materials Today Physics (2023) 100969.
- [63] M.A. Moreno-Mateos, J. Gonzalez-Rico, E. Nunez-Sardinha, C. Gomez-Cruz, M.L. Lopez-Donaire, S. Lucarini, A. Arias, A. Muñoz-Barrutia, D. Velasco, D. Garcia-Gonzalez, Magneto-mechanical system to reproduce and quantify complex strain patterns in biological materials, Appl. Mater. Today 27 (2022) 101437.
- [64] C. Dorn, L. Bodelot, K. Danas, Experiments and numerical implementation of a boundary value problem involving a magnetorheological elastomer layer subjected to a nonuniform magnetic field, J. Appl. Mech. 88 (7) (2021).
- [65] S. Yang, P. Sharma, A tutorial on the stability and bifurcation analysis of the electromechanical behaviour of soft materials, Applied Mechanics Reviews 75 (4) (2023) 044801.
- [66] B. Yi, Y. Zhou, G.H. Yoon, K. Saitou, Topology optimization of functionally-graded lattice structures with buckling constraints, Comput. Methods Appl. Mech. Engrg. 354 (2019) 593–619.
- [67] C.F. Christensen, F. Wang, O. Sigmund, Multiscale topology optimization considering local and global buckling response, 2022, http://dx.doi.org/10.48550/ARXIV.2210.11477, arXiv URL https://arxiv.org/abs/2210.11477.